INSTITUTE FOR FUSION STUDIES

DE-FG03-96ER-54346-773 IFSR #773

Nonlinear Interaction of Fast Particles with Alfvén Waves in Toroidal Plasmas

J. CANDY,† D. BORBA,‡ G.T.A. HUYSMANS, W. KERNER
JET Joint Undertaking
Abingdon, Oxfordshire OX14 3EA
United Kingdom

† Present address: IFS, The Univ. of Texas at Austin, Austin, TX 78712, USA
‡ Permanent address: Associacão EURATOM/IST, Av Rovisco Pais 1096 Lisbon, Portugal

January 1997

THE UNIVERSITY OF TEXAS

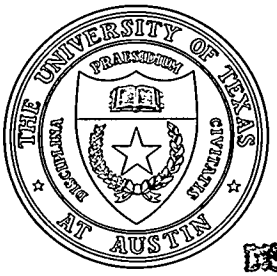

AUSTIN

DISCLAIMER

Nonlinear Interaction of Fast Particles with Alfvén Waves in Toroidal Plasmas

J. CANDY[†], D. BORBA[‡], G.T.A. HUYSMANS, W. KERNER

JET Joint Undertaking
Abingdon, Oxfordshire OX14 3EA, United Kingdom

H.L. BERK

Institute for Fusion Studies
The University of Texas at Austin, Austin, Texas 78712, U.S.A.

Abstract

A numerical algorithm to study the nonlinear, resonant interaction of fast particles with Alfvén waves in tokamak geometry has been developed. The scope of the formalism is wide enough to describe the nonlinear evolution of fishbone modes, toroidicity-induced Alfvén eigenmodes and ellipticity-induced Alfvén eigenmodes, driven by both passing and trapped fast ions. When the instability is sufficiently weak, it is known that the wave-particle trapping nonlinearity will lead to mode saturation before wave-wave nonlinearities are appreciable. The spectrum of *linear* modes can thus be calculated using a magnetohydrodynamic normal-mode code, then nonlinearly evolved in time in an efficient way according to a two-time-scale Lagrangian dynamical wave model. The fast particle kinetic equation, including the effect of orbit nonlinearity arising from the mode perturbation, is simultaneously solved for the deviation, $\delta f = f - f_0$, from an initial analytic distribution f_0. High statistical resolution allows linear growth rates, frequency shifts, resonance broadening effects, and nonlinear saturation to be calculated quickly and precisely. The results have been applied to an ITER instability scenario. Results show that weakly-damped core-localized modes alone cause negligible alpha transport in ITER-like plasmas – even with growth rates one order of magnitude higher than expected values. However, the possibility of significant transport in reactor-type plasmas due to weakly unstable global modes remains an open question.

[†]Present address: Institute for Fusion Studies, The University of Texas at Austin, Austin, TX 78712, USA

[‡]Permanent address: Associação EURATOM/IST, Av Rovisco Pais 1096 Lisbon, Portugal

17 December 1996

I. Introduction

A critical requirement for the design of a steady-state fusion reactor is good confinement of the fusion-product alpha particles, with a substantial transfer of the alpha energy back into the bulk plasma. The design specification for the proposed ITER device [1] requires that the alpha particle loss be less than 5% of the total alpha particle energy. This is equivalent to an energy loss rate of less than 20 MW. It is already known that some fraction of the alpha particles will be lost due to toroidal field ripple, but for nominal ITER plasma currents and expected edge temperatures of 3-6 keV, the loss fraction has been estimated to be quite small (less than 1%). However, it was pointed out more than two decades ago [2-3] that the substantial free energy of the alpha particle population represents a mechanism for the excitation of Alfvén waves. Various types of discrete Alfvén eigenmodes (AE) have been predicted to exist in tokamak plasmas — for example, the global (GAE), toroidal (TAE), kinetic (KTAE), elliptic (EAE), noncircular (NAE) and beta (BAE) Alfvén eigenmodes. Most of the experimental and analytical effort has been devoted to the study of TAE modes, which have been clearly observed in a variety of experiments, either passively driven by neutral beam injection (NBI) [4-5] and ion-cyclotron-resonance heating (ICRH) [6], or actively excited by external antennae [7]. More recently, alpha-driven TAE activity has been observed in burning D-T plasmas [8].

The fear is that if these modes are driven unstable by resonant interaction with alpha particles in a reactor-type plasma, and if nonlinear saturation of the unstable spectrum occurs at a sufficiently high amplitude, anomalous transport and/or loss resulting from the stochastic motion of the alphas may result. The first step in the systematic analysis of the alpha transport scenario has been the study of the linear aspects of the problem; namely, eigenmode structures and damping rates, in both large-aspect-ratio and general toroidal geometry. Further, perturbative and semi-perturbative calculations of the background damping due to thermal electrons and ions have been accomplished both analytically and numerically [9-12]. It has been accepted for some time that for a large, high-field machine the range of toroidal mode numbers, n, for which TAEs are likely to be unstable can be very large. In particular, simulations using a linear boundary layer model [13] showed that for ITER-like plasmas [14], this range could be as large as $10 \lesssim n \lesssim 50$ (*cf.*, Fig. 1). The calculation of the linear mode structure as well as the nonlinear evolution of such a broad spectrum of high-n modes turns out, not surprisingly, to be substantially more complex than for a few low-n modes.

In the present paper we summarize the underlying physical principles, as well as various technical aspects, of a new numerical technique to study the nonlinear phase of Alfvén wave evolution in tokamaks – including self-consistent anomalous fast-ion transport. Subsequently, we apply this model to an ignited ITER-like plasma.

We emphasize that the approach is based largely on the methodology of Refs. 15-17, for which the relevant nonlinearity is the trapping of resonant particles in the

finite-amplitude Alfvén wave field. This assumption has been discussed exhaustively in previous literature [18-20] for the TAE problem, and has also been validated by full gyro-kinetic-MHD hybrid simulations [20]. A necessary condition for the predominance of the wave-particle nonlinearity is a small fractional growth rate (roughly $\gamma_L/\omega \sim 10^{-2}$). Indeed, if this condition is satisfied, the wave will grow to a saturated state with negligibly small wave-wave nonlinearity. It is precisely this sort of weakly-unstable regime that appears to be characteristic of AE modes in ITER-like plasmas. The linearity of the background plasma response enables a substantial reduction of computational complexity, since the fluid modes can be taken directly from a linear eigenvalue code such as CASTOR-CR [21].

As the fast particle pressure grows beyond a critical value, non-perturbative unstable modes can exist [22]. These so-called energetic particle modes (EPM) are not considered in the present work, although it is known that they can have a strong scaling of γ_L with the fast ion pressure, and thus a potentially large saturated amplitude.

An overriding complication of the linear theory is the strong sensitivity of the mode structure and damping rate to the plasma equilibrium – and in particular to the safety factor. This complexity will dictate our simulation methodology, as described in the sections which follow.

II. Fast Particle Motion

A. Guiding center Hamiltonian

Fast ion trajectories in an axisymmetric toroidal plasma can be approximated by the gyro-averaged motion of the particle guiding center so long as the gyro-radius, ρ_f, is sufficiently small and the perturbing wave frequency, ω, is low:

$$\frac{1}{B}\frac{dB}{dr}\rho_f \ll 1 \qquad \text{and} \qquad \omega \ll \omega_{\text{ci}} \tag{1}$$

In Eq. (1), B is the magnetic field amplitude, r is the minor radius, and ω_{ci} is the ion cyclotron frequency. When the preceding conditions are satisfied, the resonant interaction between waves and particles is dominated by the transit motion of the guiding center in the TAE case, or the toroidal drift motion of the banana/potato center in the fishbone case.

The Hamiltonian for n_p guiding-center particles (index j) moving in a spectrum of n_w fixed-amplitude Alfvén waves (index k) is

$$H_{\text{gc}} = \sum_{j=1}^{n_p} m\left(\frac{1}{2}v_{\|j}^2 + \mu_j B_j + \frac{e}{m}\Phi_j\right) . \tag{2}$$

where e and m are the particle charge and mass, respectively, and $\mu_j = v_{\perp j}^2/2B_j$ is the constant magnetic moment of the jth particle. Technically, we are interested in the flow of the fast particle canonical phase space, rather than the motion of individual particles themselves, so that we hereafter refer to the index j as the label of a "marker" in phase-space. While the two pictures are essentially equivalent in regards to the path traced by the jth phase point, the effective number of particles associated with each marker may change with time.

B. Magnetic field representation

The simple appearance of Eq. (2) is deceptive, in fact, as it contains no information about the equilibrium magnetic field structure, and makes no explicit reference to canonical variables. To make the Hamiltonian formulation explicit, we must first decide on an appropriate set of coordinates for the magnetic field representation.

For an axisymmetric toroidal equilibrium, we begin with the standard form

$$\mathbf{B} = g(\psi)\nabla\zeta + \nabla\zeta \times \nabla\psi \, , \tag{3}$$

where ψ is the poloidal flux and ζ is the (physical) toroidal angle. Following the method presented in Ref. 23, to which the reader is referred for a complete derivation, we introduce the new (nonphysical) *toroidal* angle

$$\varphi \equiv \zeta - \nu(\theta, \psi) \ , \tag{4}$$

with θ an undetermined angle in the *poloidal* cross-section. The goal of the transformation defined by Eq. (4) is to choose the function ν so that the field lines in the (θ, φ)-plane are straight. With ν suitably chosen [23] the magnetic field can then be written in the geometrically intuitive form

$$\mathbf{B} = \nabla(\varphi - q\theta) \times \nabla\psi \ , \tag{5}$$

with the safety factor,

$$q(\psi) = \frac{\mathbf{B} \cdot \nabla\varphi}{\mathbf{B} \cdot \nabla\theta} = \frac{d\chi(\psi)}{d\psi} \ , \tag{6}$$

constant on a magnetic surface, and $\chi(\psi)$ the toroidal flux. The freedom which remains in choosing the poloidal angle θ can be equivalently viewed as a freedom to choose the Jacobian, $\mathcal{J}$, connecting toroidal coordinates to real-space variables. Note that while $\mathcal{J}$ depends on the choice of poloidal angle, it is independent of how we shift the toroidal angle (*cf.*, Eq. (4)):

$$\mathcal{J} = \frac{1}{|\nabla\psi \cdot (\nabla\theta \times \nabla\zeta)|} = \frac{1}{|\nabla\psi \cdot (\nabla\theta \times \nabla\varphi)|} \ . \tag{7}$$

It is shown in Ref. 23 that if the quantity $\mathcal{J}B^2$ is chosen as a flux function then the covariant representation of the magnetic field becomes especially simple. Indeed, $\mathbf{B}$ takes the form

$$\mathbf{B} = g(\psi)\nabla\varphi + I(\psi)\nabla\theta + \delta(\psi, \theta)\nabla\psi \ , \tag{8}$$

with $I(\psi)$ independent of θ for the specific choice

$$\mathcal{J}B^2 = I(\psi) + g(\psi)q(\psi) \ . \tag{9}$$

Despite the appearance of the nonzero radial component of $\nabla\psi$ in Eq. (8), it is clear from Eq. (5) that the magnetic field satisifes the obvious requirement that $\mathbf{B} \cdot \nabla\psi = 0$. This completes the specification of the coordinate system for the guiding center motion. With the magnetic field expressed as in Eq. (8), the Hamiltonian will depend only the quantities g, I, q, and B. For reference, we note that a vector potential corresponding to this field is $\mathbf{A} = \chi\nabla\theta - \psi\nabla\varphi$.

In Eq. (2), the indices on the magnetic field strength $B(\psi,\theta)$ and electrostatic potential $\Phi(\psi,\theta,\varphi)$ indicate that they are to be evaluated at the location $(\psi_j,\theta_j,\varphi_j)$ of the jth particle.

C. Structure of the perturbation

Within the context of linear theory, a distinct toroidal eigenfunction (index k, mode number n_k) is written as a sum over all poloidal harmonics (mode number m). For a nonlinear simulation, however, only the dominant poloidal harmonics need be retained. In its most general form, then, the full potential at the jth particle position is written as sum over eigenfunctions with slowly varying amplitudes:

$$\frac{e}{m}\Phi_j = \sum_{k=1}^{n_w} \sum_{m=m_k^-}^{m_k^+} \left[\mathcal{X}_k(t)\cos\Theta_{jkm} + \mathcal{Y}_k(t)\sin\Theta_{jkm}\right]\phi_{km}(\psi_j)\ , \tag{10}$$

where the phase angle, Θ_{jkm}, is defined as

$$\Theta_{jkm} \equiv n_k\varphi_j - m_k\theta_j - \omega_k t\ . \tag{11}$$

The amplitudes $\mathcal{X}_k$ and $\mathcal{Y}_k$ – undetermined by linear theory – are to be determined by the nonlinear model. In Eq. (11) and in what follows, ω_k refers only to the real part of the frequency of the kth eigenmode.

An adequate description of the spatial structure of the unstable modes can be realized by representing magnetic perturbations in the following restricted fashion:

$$\delta\mathbf{B} = \nabla\times(\delta\mathbf{A}_\parallel) \to \nabla\times(\alpha\mathbf{B})\ . \tag{12}$$

The perturbation is thus characterized by the pair (Φ,α), which are both first-order quantities (although a δ prefix has not been used). We emphasize that Eq. (12) is a convenient description in that the parallel momentum (see Ref. 23) becomes

$$\rho_j = \frac{v_{\parallel j}}{B_j} + \alpha_j\ . \tag{13}$$

Eq. (12) also gives an appropriate description of low-β shear Alfvén waves, for which $\delta E_\parallel = 0$ and

$$\frac{1}{c}\frac{\partial\delta\mathbf{A}_\parallel}{\partial t} = -\mathbf{b}\cdot\nabla\Phi\ . \tag{14}$$

The connection between Φ and $\delta\mathbf{A}_\parallel$ above implies that α in Eq. (12) is strictly determined by the functional form of Φ for the low-β case. In Eq. (14), $\mathbf{b}\equiv\mathbf{B}/B$ is the unit vector along the equilibrium magnetic field. For convenience, we choose the system of units shown in Table I, so that α_j may be written

$$\alpha_j = \frac{1}{B_j} \sum_{k=1}^{n_w} \sum_{m=m_k^-}^{m_k^+} \frac{k_{\parallel m}}{\omega_k} \left[\mathcal{X}_k(t) \cos\Theta_{jkm} + \mathcal{Y}_k(t) \sin\Theta_{jkm} \right] \phi_{km}(\psi_j) \ . \tag{15}$$

The canonical toroidal and poloidal angular momenta have the explicit, compact forms

$$P_{\varphi j} = g_j \rho_j - \psi_j \ , \tag{16a}$$
$$P_{\theta j} = I_j \rho_j + \chi_j \ , \tag{16b}$$

with ρ_j defined in terms of the perturbation α_j (see Eq. (13)). Eliminating $v_{\parallel j}$ in Eq. (2) using Eq. (13) gives

$$\begin{aligned} H_{\rm gc}\left(\{P_{\varphi j}, \varphi_j, P_{\theta j}, \theta_j\}, t\right) &= \sum_{j=1}^{n_p} \left[\frac{1}{2} (\rho_j - \alpha_j)^2 B_j^2 + \mu_j B_j + \Phi_j \right] \ , \\ &= \sum_{j=1}^{n_p} H_j \ , \end{aligned} \tag{17}$$

such that $\rho_j = \rho_j(P_{\varphi j}, P_{\theta j})$ and $\psi_j = \psi_j(P_{\varphi j}, P_{\theta j})$. Hamilton's equations, which follow at once from Eq. (17), are

$$\dot{P}_{\varphi j} = v_{\parallel j} \alpha_{\varphi j} - \Phi_{\varphi j} \ , \tag{18a}$$
$$\dot{P}_{\theta j} = v_{\parallel j} \alpha_{\theta j} - \Phi_{\theta j} - \left(v_{\parallel j}^2 + \mu_j B_j \right) \frac{1}{B_j} \frac{\partial B_j}{\partial \theta_j} \ , \tag{18b}$$
$$\dot{\varphi}_j = \frac{v_{\parallel j} B_j}{D_j} \left(q_j + \rho_j \frac{\partial I_j}{\partial \psi_j} \right) + \frac{I_j}{D_j} \Lambda_j \ , \tag{18c}$$
$$\dot{\theta}_j = \frac{v_{\parallel j} B_j}{D_j} \left(1 - \rho_j \frac{\partial g_j}{\partial \psi_j} \right) - \frac{g_j}{D_j} \Lambda_j \ , \tag{18d}$$

$$\text{with} \qquad \Lambda_j \equiv v_{\parallel j} \alpha_{\psi j} - \Phi_{\psi j} - \left(v_{\parallel j}^2 + \mu_j B_j \right) \frac{1}{B_j} \frac{\partial B_j}{\partial \psi_j} \ , \tag{19}$$

$$\text{and} \qquad D_j \equiv \rho_j \left(g_j \frac{\partial I_j}{\partial \psi_j} - I_j \frac{\partial g_j}{\partial \psi_j} \right) + I_j + q_j g_j \ . \tag{20}$$

The various partial derivatives of Φ and α are given explicitly in Appendix A.

In practice, it is more convenient to integrate ψ_j forward in time and then evaluate $P_{\theta j}$ explicitly using Eq. (16b), rather than evolve $P_{\theta j}$ forward and attempt to invert Eq. (16a) for ψ_j. In terms of differential quantities, the equation for $\dot{\psi}_j$ is

$$\dot{\psi}_j = \frac{g_j}{D_j}\dot{P}_{\theta j} - \frac{I_j}{D_j}\dot{P}_{\varphi j} \ . \tag{21}$$

D. Wave evolution

A Lagrangian representation for the time-evolution of free (undriven) Alfvén waves has been considered previously in Ref. 24. For the evolution of linear, fluid Alfvén waves – which are assumed to grow on a timescale asymptotically longer than the equilibrium – the structure of this Lagrangian is universal:

$$\mathcal{L}_{\rm w} = \mathcal{L}_{\rm w}^{(0)}(\omega_0) + \mathcal{L}_{\rm w}^{(1)} \ . \tag{22}$$

Variation of $\mathcal{L}_{\rm w}^{(0)}$ gives the fluid eigenmode structure, whereas variation of $\mathcal{L}_{\rm w}^{(1)}$ gives the slow time evolution of the mode. Time derivatives in subsequent formulae refer to the slow (wave growth) timescale

$$\frac{\partial}{\partial t} \sim \gamma \ll \omega_0 \ . \tag{23}$$

Thus, in an operational sense, one fixes the spatial structure of the eigenmode and allows time variation of the amplitude – which is undetermined by linear theory. The nature of the approximation is analogous to the perturbative δW formulation of Ref. 18, although the present formulation includes the wave amplitude and phase as intrinsic dynamical variables. Hereafter we omit the superscript 1 from the perturbed wave Lagrangian, which has the general form

$$\mathcal{L}_{\rm w}^{(1)} = \sum_{k=1}^{n_w} \frac{\mathrm{E}_k}{\omega_k^2}\left[\dot{\mathcal{X}}_k^2 + \dot{\mathcal{Y}}_k^2 + \omega_k\left(\mathcal{X}_k\dot{\mathcal{Y}}_k - \dot{\mathcal{X}}_k\mathcal{Y}_k\right)\right] \ , \tag{24}$$

with E_k the inertial energy per unit amplitude of a shear-Alfvén wave:

$$\mathrm{E}_k = \frac{c^2}{8\pi}\frac{m^2}{e^2}\int \frac{dV}{v_{\rm A}^2}|\nabla_\perp \Phi^{(k)}|^2 \qquad \text{[Gaussian units]} \ . \tag{25}$$

The integral in Eq. (24) is defined completely by the linear eigenmode structure:

$$\Phi^{(k)} \equiv \sum_{m=m_k^-}^{m_k^+} \exp\left[i(n_k\varphi - m\theta)\right]\, \phi_{km}(\psi) \ . \tag{26}$$

We also note that in the large-aspect-ratio, constant density limit, one may simplify the expression for E_k substantially. To leading order $dV \sim rR_0 dr\, d\varphi\, d\theta$, so that in normalized units the wave energy is

$$\mathrm{E}_k \sim 2\pi^2 \mathrm{n_i m_i} \int_0^1 x\,dx \sum_{m=m_k^-}^{m_k^+} \left[\left(\frac{d\phi_{km}}{dx} \right)^2 + \left(\frac{m\phi_{km}}{x} \right)^2 \right] , \tag{27}$$

with $x \equiv r/a$ the normalized minor radius. Here, $\mathrm{n_i}$ is the thermal ion density, measured in units of $1/R_0^3$, and $\mathrm{m_i}$ is the ion mass, measured in units of the fast particle mass. The interaction Lagrangian, which is already implicitly contained in the guiding-center Hamiltonian, Eq. (17), is also needed to determine the wave evolution. For a zero-β perturbation, this takes the form is

$$\mathcal{L}_{\mathrm{int}} = -\sum_{j=1}^{n_p} \sum_{k=1}^{n_w} \sum_{m=m_k^-}^{m_k^+} \frac{(\omega_k - k_{\parallel m} v_{\parallel j})}{\omega_k} \left(\mathcal{X}_k \cos\Theta_{jkm} + \mathcal{Y}_k \sin\Theta_{jkm} \right) \phi_{km}(\psi_j) , \tag{28}$$

which has been discussed previously in Ref. 25. Variation of $\mathcal{L}_{\mathrm{int}} + \mathcal{L}_{\mathrm{w}}$ then yields the extremal equations

$$\dot{\mathcal{X}}_k = \frac{\omega_k}{2\mathrm{E}_k} \frac{\partial \mathcal{L}_{\mathrm{int}}}{\mathcal{Y}_k} = -\frac{1}{2\mathrm{E}_k} \sum_{j=1}^{n_p} \sum_{m=m_k^-}^{m_k^+} (\omega_k - k_{\parallel m} v_{\parallel j}) \sin\Theta_{jkm}\, \phi_{km}(\psi_j) , \tag{29a}$$

$$\dot{\mathcal{Y}}_k = -\frac{\omega_k}{2\mathrm{E}_k} \frac{\partial \mathcal{L}_{\mathrm{int}}}{\mathcal{X}_k} = \frac{1}{2\mathrm{E}_k} \sum_{j=1}^{n_p} \sum_{m=m_k^-}^{m_k^+} (\omega_k - k_{\parallel m} v_{\parallel j}) \cos\Theta_{jkm}\, \phi_{km}(\psi_j) , \tag{29b}$$

where we have neglected second derivatives of $\mathcal{X}_k$ and $\mathcal{Y}_k$ which arise from the first two terms of $\mathcal{L}_{\mathrm{w}}$ in Eq. (24). This simplification is consistent with the assumption of slow variation of the linear eigenmode amplitude.

E. System Invariants

At this point, we can derive conservation relations for both the energy and the momentum of the coupled wave-particle system. First, the rate of change of toroidal canonical momentum, $\dot{P}_{\varphi j}$, as a sum over individual wave contributions is

$$\dot{P}_{\varphi j} = \sum_{k=1}^{n_w} \dot{P}_{\varphi jk}$$

$$\text{with} \quad \dot{P}_{\varphi jk} \equiv \frac{n_k}{\omega_k} \sum_{m=m_k^-}^{m_k^+} (\omega_k - k_{\parallel m} v_{\parallel j}) \left[\mathcal{X}_k \sin\Theta_{jkm} - \mathcal{Y}_k \cos\Theta_{jkm} \right] \phi_{km}(\psi_j) , \tag{30}$$

while the rate of change of particle energy is

$$\dot{H}_{\rm gc} = \frac{\partial H_{\rm gc}}{\partial t} = \sum_{j=1}^{n_p} \sum_{k=1}^{n_w} \frac{\omega_k}{n_k} \dot{P}_{\varphi jk} \ . \tag{31}$$

It should be mentioned that cross-terms which arise from the amplitude variation

$$\dot{\mathcal{X}}_k \frac{\partial H_{\rm gc}}{\mathcal{X}_k} \qquad \text{and} \qquad \dot{\mathcal{Y}}_k \frac{\partial H_{\rm gc}}{\mathcal{Y}_k} \ , \tag{32}$$

vanish when summed over particles. Further, it can be verified that

$$\begin{aligned} & 2{\rm E}_k \left(\mathcal{X}_k \dot{\mathcal{X}}_k + \mathcal{Y}_k \dot{\mathcal{Y}}_k \right) \\ & \quad = -\sum_{j=1}^{n_p} \sum_{m=m_k^-}^{m_k^+} (\omega_k - k_{\parallel m} v_{\parallel j}) \left[\mathcal{X}_k \sin\Theta_{jkm} - \mathcal{Y}_k \cos\Theta_{jkm} \right] \phi_{km}(\psi_j) \\ & \quad = \sum_{j=1}^{n_p} \frac{\omega_k}{n_k} \dot{P}_{\varphi jk} \ . \end{aligned} \tag{33}$$

Summing Eq. (33) over k and comparing with Eq. (31), yields the conservation of energy relation

$$\frac{d}{dt} \left(H_{\rm gc} + {\rm E}_{\rm wave} \right) = 0 \ . \tag{34}$$

Here we have defined the wave energy, $\rm E_{wave}$, as

$${\rm E}_{\rm wave} \equiv \sum_{k=1}^{n_w} {\rm E}_k A_k^2 \qquad \text{with} \qquad A_k^2 \equiv \mathcal{X}_k^2 + \mathcal{Y}_k^2 \ . \tag{35}$$

By a similar calculation, it is simple to show that momentum is also conserved:

$$\frac{d}{dt} \left({\rm P}_{\rm particle} + {\rm P}_{\rm wave} \right) = 0 \ , \tag{36}$$

where the particle and wave momenta are, respectively,

$${\rm P}_{\rm particle} \equiv \sum_{j=1}^{n_p} P_{\varphi j} \qquad \text{and} \qquad {\rm P}_{\rm wave} \equiv \sum_{k=1}^{n_w} \frac{n_k}{\omega_k} {\rm E}_k A_k^2 \ . \tag{37}$$

In the case of only one Alfvén eigenmode ($n_w = 1$), the momentum and energy equations are formally degenerate, and differ only by the constant ω/n.

III. Algorithm for Numerical Simulation

A. Discretization of the kinetic equation

The differential element of phase space volume in straight-line field coordinates is normally written as

$$d\Gamma^{(p)} = 2\pi v^2\, dv\, d\lambda\, \mathcal{J}\, d\psi\, d\varphi\, d\theta\ , \tag{38}$$

where $\lambda \equiv v_\parallel/v$ is the cosine of the pitch angle, and $\mathcal{J}$ is the Jacobian defined in Eqs. (7) and (9). The volume element associated with the Hamiltonian flow generated by $H_{\rm gc}$ is

$$d\Gamma = (2\pi d\mu)(dP_\varphi\, d\varphi)(dP_\theta\, d\theta)\ . \tag{39}$$

Note that $\Gamma^{(p)}$ — which refers to the *physical* phase space — is not in general equal to the invariant volume element Γ associated with the flow $H_{\rm gc}$. The transformation rule between the two is

$$d\Gamma^{(p)} = \mathcal{N} d\Gamma\ , \tag{40}$$

where $\mathcal{N}$ is the determinant of the Jacobian matrix.

$$\mathcal{N} \equiv \left|\frac{\partial\Gamma^{(p)}}{\partial\Gamma}\right| \sim 1 + \mathcal{O}\left(\frac{v_\parallel}{\omega_{\rm ci} R_0}\right)\ . \tag{41}$$

This means that with regard to the guiding-center motion, $\Gamma^{(p)}$ is a weak function of time. In what follows we will therefore restrict our attention to the canonical element Γ for purposes of numerical simulation, since exact time-invariance of the volume element is an algorithmic requirement.

In the absence of a plasma wave ($\mathcal{X}_k = \mathcal{Y}_k = 0$), the fast particle motion will conserve both the energy, $H_{\rm gc}$, and toroidal momentum, P_φ. Additionally, the magnetic moment, μ, is exactly conserved, regardless of the size of the perturbation. The unperturbed distribution of fast particles is accordingly restricted to be a function of these motion invariants.

It is well-known that the δf-method is the most efficient technique to evolve the fast ion distribution forward in time. We employ the algorithm developed in Ref. 26, with the subtle modifications described below. Begin by writing the fast-ion distribution f in the form

$$f = \underbrace{f_0(\mathcal{E}, \mathcal{P}_\varphi; \mu)}_{\text{equilibrium}} + \underbrace{\delta f_{\rm a}(\Gamma, t)}_{\text{fluid-like}} + \underbrace{\delta f_{\rm na}(\Gamma, t)}_{\text{kinetic}} \ . \tag{42}$$

where $\mathcal{P}_\varphi$ and $\mathcal{E}$ are the *unperturbed* momentum and energy, respectively:

$$\begin{aligned} \mathcal{P}_\varphi &= \frac{g v_\parallel}{B} - \psi \\ &= P_\varphi - \alpha g \end{aligned} \qquad \text{and} \qquad \begin{aligned} \mathcal{E} &= \frac{v_\parallel^2}{2} + \mu B \\ &= H - \Phi \end{aligned} \ . \tag{43}$$

The equilibrium part, f_0, which is to be specified analytically, defines the total number of particles through a simple moment:

$$n_0 \equiv \int f_0(\mathcal{E}, \mathcal{P}_\varphi; \mu)\, d\Gamma \ . \tag{44}$$

The adiabatic part, $\delta f_{\rm a}$, is responsible for the fluid-like contribution to the fast-ion response [27-28].

$$\delta f_{\rm a} = \alpha g \frac{\partial f_0}{\partial \mathcal{P}_\varphi} + \Phi \frac{\partial f_0}{\partial \mathcal{E}} \ . \tag{45}$$

For this reason, it is appropriate within the context of the two-time-scale formalism to consider the adiabatic response as accounted for in the fluid eigenmode structure, even if in practice it is neglected. Thus we are interested in the time evolution of $\delta f_{\rm na}$ only. Substituting f, as written in Eq. (42), into the kinetic equation $df/dt = 0$ gives an evolution equation for the nonadiabatic response

$$\frac{d\delta f_{\rm na}}{dt} = -\dot{P}_\varphi \frac{\partial f_0}{\partial \mathcal{P}_\varphi} - \dot{H} \frac{\partial f_0}{\partial \mathcal{E}} \ . \tag{46}$$

In order to represent $\delta f_{\rm na}$ numerically, we begin by specifying a 5-dimensional cube $\mathcal{U}$ inside of which markers are to be loaded in an asymptotically *uniform* way. This is done systematically with the use of a bit-reveral scheme described in Ref. 26. An element of volume in $\mathcal{U}$ is then related to the corresponding element in Γ through

$$d\Gamma = \mathcal{M}\, d\mathcal{U} \ , \tag{47}$$

where $\mathcal{M}$ is the determinant of the Jacobian transformation matrix. It should be clear that the choice of $\mathcal{U}$ is *not* unique and may be altered to suit a particular simulation. A simple but effective choice is

$$d\mathcal{U} = d\psi\, dv\, d\lambda\, d\varphi\, d\theta \ . \tag{48}$$

For clarity, the relevant volume elements and Jacobian determinants are summarized in Table II. We mention, also, that the loading defined in Eq. (48) is not necessarily optimal. For example, loading uniformly in $\psi^{1/2}$, rather than in ψ, may result in faster convergence with increasing marker number.

Once the space $\mathcal{U}$ is specified, we partition it into n_p equal-volume hypercubes (with centers computed using the bit-reversal technique). Referring to Eq. (47), we find that the *time-independent* volume in Γ corresponding to the jth $\mathcal{U}$-hypercube is

$$\Delta\Gamma_j \equiv \frac{V(\mathcal{U})}{n_p}\,\mathcal{M}_j \qquad \text{with} \qquad V(\mathcal{U}) = \int d\mathcal{U}\ , \tag{49}$$

with the Jacobian $\mathcal{M}$ evaluated at $t = 0$ to reflect the invariance of $\Delta\Gamma_j$ in time. The density of particles on each element $\Delta\Gamma_j$ satisifes the discrete version of Eq. (46):

$$\frac{d\delta f_{\mathrm{na}j}}{dt} = -\dot{P}_{\varphi j}\left.\frac{\partial f_0}{\partial \mathcal{P}_\varphi}\right|_j - \dot{H}_j\left.\frac{\partial f_0}{\partial \mathcal{E}}\right|_j . \tag{50}$$

With the definitions presented above, we can change between integrals and particle sums according to

$$\int f(\Gamma,t)g(\Gamma,t)\,d\Gamma \sim \int f_0(\Gamma)g(\Gamma,t)d\Gamma + \sum_{j=1}^{n_p}\delta n_j(t)\,g(\Gamma_j(t),t)\ . \tag{51}$$

where $\delta n_j(t) \equiv \Delta\Gamma_j\,\delta f_{\mathrm{na}j}(t)$. Eq. (51) clearly introduces a discretization error, but uniformly approaches the continuum limit as $n_p \to \infty$. Finally, applying the transformation rule, Eq. (51), to the wave equations and introducing a linear background wave damping rate γ_{d}, we obtain

$$\dot{\mathcal{X}}_k = -\frac{1}{2\mathrm{E}_k}\sum_{j=1}^{n_p}\delta n_j \sum_{m=m_k^-}^{m_k^+}(\omega_k - k_{\|m}v_{\|j})\,\sin\Theta_{jkm}\phi_{km}(\psi_j) - \gamma_{\mathrm{d}}\,\mathcal{X}_k\ , \tag{52a}$$

$$\dot{\mathcal{Y}}_k = \frac{1}{2\mathrm{E}_k}\sum_{j=1}^{n_p}\delta n_j \sum_{m=m_k^-}^{m_k^+}(\omega_k - k_{\|m}v_{\|j})\,\cos\Theta_{jkm}\phi_{km}(\psi_j) - \gamma_{\mathrm{d}}\,\mathcal{Y}_k\ . \tag{52b}$$

This completes the derivation of the nonlinear model. The result, which we summarize for completeness below, is a $(5 \times n_p + 2 \times n_w)$–dimensional system of ordinary differential equations.

$$\left\{\begin{array}{c}\dot{P}_{\varphi j}\\ \dot{\psi}_j\\ \dot{\varphi}_j\\ \dot{\theta}_j\\ \delta\dot{f}_j\end{array}\right\} \quad j=1,\ldots,n_p \qquad \left\{\begin{array}{c}\dot{\mathcal{X}}_k\\ \dot{\mathcal{Y}}_k\end{array}\right\} \quad k=1,\ldots,n_w \tag{53}$$

This algorithm has been coded in FORTRAN, and compiled on a variety of platforms. It has been given the name FAC, for **F**ast particle, **A**lfvén wave interaction **C**ode.

B. Orbit averaging method

According to Eq. (42), we must specify the distribution as a function of $\mathcal{P}_\varphi$ and $\mathcal{E}$. Of course, analytical approximations to f_0, for both trapped and passing particles, are typically formulated in the zero-orbit-width limit (*e.g.*, Ref. 29), for which the poloidal flux is constant along a particle orbit. However, for particles with MeV-range energies, the excursion from a flux surface can be a substantial fraction of the machine size. Passing alphas in JET, for example, can have Δ_b/a in excess of 1/4, where Δ_b is the orbit width.

Consider, for example, the consequence of writing the equilibrium distribution as $f_0(\psi,\mathcal{E})$. Such a form would require Eq. (46) to be recast as

$$\delta\dot{f}_{\rm na} = -\dot{\psi}\frac{\partial f_0}{\partial\psi} - \dot{H}\frac{\partial f_0}{\partial\mathcal{E}}\ , \tag{54}$$

Clearly, f_0 would *not* be a stationary distribution in the limit $\mathcal{X}_k,\mathcal{Y}_k\to 0$, as $\delta f_{\rm na}$ would be modified according to the finite drift velocity $\dot{\psi}$. The essential point is that unless f_0 is expressed as a function of the true constants of motion, statistical noise in $\delta f_{\rm na}$ will *not* scale with the amplitude of the perturbation. Thus, it is an absolute computational requirement that f_0 have the form indicated in Eq. (42). However, this is a rather inconvenient requirement, with the consequent form of the distribution rather unintuitive. Also, experimental measurments of quantities which determine the fast-particle profile — such as radial deposition profiles in the case of neutral beam injection — give results naturally in terms of the poloidal flux. Thus, we need to develop a general procedure to obtain a *realistic* distribution $f_0(\mathcal{P}_\varphi,\mathcal{E};\mu)$ from a given *reference* zero-orbit-width distribution $F(\psi,\mathcal{E})$.

The goal is, quite simply, to obtain a reasonable expression for an *averaged* quantity $\langle\psi\rangle$ that is a function only of constants of motion. From a physical standpoint, then, $\langle\psi\rangle$ labels what is effectively the "orbit center" of a particle with given $(\mathcal{E},\mathcal{P}_\varphi,\mu)$ and arbitrarily large orbit excursion. Using the equation defining $\mathcal{P}_\varphi$ in Eq. (43), we can write the averaging condition as

$$\langle\psi\rangle = \left\langle \frac{g(\psi)\sigma}{B}\sqrt{2(\mathcal{E}-\mu B)}\right\rangle - \mathcal{P}_\varphi\ , \tag{55}$$

where $B = B(\psi, \theta)$ and σ is the sign of $v_\parallel$. For trapped particles, the parallel velocity changes sign at the banana tip. The value of ψ at this point is thus a good indicator of the orbit average: $\langle\psi\rangle = -\mathcal{P}_\varphi$. A simple map valid for all classes of particles in a large-aspect-ratio field is

$$\langle\psi\rangle = \begin{cases} \sqrt{\mathcal{E}-\mu} - \mathcal{P}_\varphi & \mathcal{E} > \mu \quad \text{(co-passing)} \\ -\mathcal{P}_\varphi & \mathcal{E} < \mu \\ -\sqrt{\mathcal{E}-\mu} - \mathcal{P}_\varphi & \mathcal{E} > \mu \quad \text{(counter-passing)} \end{cases} \tag{56}$$

More complicated forms can be derived by rigorous averaging methods, but the method described by Eq. (56) captures the essential effects of orbit excursion. Near the trapped-passing boundary, the form $\sqrt{\mathcal{E}-\mu}$ may appear to be an especially poor approximation to the average indicated in Eq. (55). However, the region where the averaging is poor is precisely where the term is essentially negligible.

Consider a passing particle with $\mu = 0$. Here, we find that the average value of ψ becomes

$$\langle\psi\rangle = v_\parallel - \mathcal{P}_\varphi \ , \tag{57}$$

where $v_\parallel = \sqrt{2\mathcal{E}}$. The correction to this expression is formally of $O(\varepsilon^2)$ if we take the average to be in poloidal angle. For the sake of illustration, let $F(\psi, \mathcal{E})$ be a typical reference beam distribution: *viz.*, exponential in poloidal flux and Maxwellian in energy. According to Eq. (57), the correspondence becomes

$$F = Ce^{-\alpha\psi}e^{-v_\parallel^2/2T} \quad \longrightarrow \quad f_0 = Ce^{-\alpha(v_\parallel - \mathcal{P}_\varphi)}e^{-v_\parallel^2/2T} \ . \tag{58}$$

The constant C in Eq. (58) may be straightforwardly related to the volume-averaged fast particle beta or the particle number by an integration over ψ in the usual manner. The requirement that the functional form be in terms of constants of motion is required only for the numerical simulation.

Finally, for illustrative purposes, we give an analytic calculation of the small-orbit-width linear growth rate in Appendix B. This derivation proceeds directly from the equations used by the numerical model, and should be particularly instructive for those not familiar with linear theory.

IV. Dynamics of Particle Trapping

A. Wave-particle resonance

If one applies first-order perturbation theory to calculate, for example, the particle orbits in a wave field of the form given by Eq. (10), a resonant denominator will occur whenever [27]

$$\Omega_\ell \equiv n\omega_\varphi - \ell\omega_\theta - \omega = 0 \qquad \ell \in Z\,. \tag{59}$$

is satisfied. Here, $\omega_\theta \equiv \langle\dot{\theta}\rangle$ is the poloidal oscillation frequency, and $\omega_\varphi \equiv \langle\dot{\varphi}\rangle$ is the frequency of motion in the toroidal direction. Particles close to this point in phase space become become trapped in the wave potential well and execute local oscillations at the wave trapping frequency, ω_t. It is interesting to note that if one attempts to calculate to second order in the perturbation, new resonances become possible; these occur when

$$\Omega_{\ell_1} + \Omega_{\ell_2} = 0\,, \tag{60}$$

such that both ℓ_1 and ℓ_2 are integers. Thus, we can say equivalently that second order resonances occur when ℓ in Eq. (59) is a half-integer. The general rule for an sth order resonance may be similarly expressed by replacing ℓ in Eq. (59) with $\ell+r/s$, where ℓ is any integer, and (r,s) are relatively prime. However, in the perturbative regime, the island size corresponding to a wave of amplitude A scales like $A^{s/2}$, so that for a small perturbation, island width vanishes rapidly as s increases.

For a realistic TAE mode scenario, energy exchange between waves and particles – and thus the instability – will saturate as a consequence of particle trapping in the relatively large $s = 1$ islands. Stochasticity, if present globally, will likely be the result of overlap of $s = 1$ islands from *different* modes, owing to the extremely small size of nonlinear islands for typical TAE saturation amplitudes.

In the one-dimensional bump-on-tail problem [30], the motion of resonant particles, which become trapped in the field of a single electrostatic wave, satisfies the nonlinear equation [31]

$$\ddot{Q} + \omega_t^2 \sin Q = 0 \qquad \text{with} \qquad Q \equiv kx - \omega t\,. \tag{61}$$

Here, (k,ω) are the wavenumber and frequency of the electrostatic mode. In this case, $\omega_t^2 = ek\mathcal{E}/m$, where $\mathcal{E}$ is the electric field amplitude of the wave. The trapping frequency grows until the wave saturates, and in the undamped, collisionless limit, the saturated state satisfies

$$c\gamma_L = \omega_t \ , \tag{62}$$

where γ_L is the linear growth rate and $c \sim 3.2$ [30] is a universal constant.

For the TAE problem, the principle mechanism which governs the saturation is similar, although the details become complicated by the higher phase space dimension. For simplicity, consider a passing population of fast ions with $\mu = 0$. In this case it is convenient to use the variable pair (p, C), where

$$p \equiv \mathcal{P}_\varphi \ , \tag{63a}$$

$$C \equiv \mathcal{E} - \frac{\omega}{n}\mathcal{P}_\varphi \ , \tag{63b}$$

In the above we have used the *unperturbed* variables $\mathcal{P}_\varphi$ and $\mathcal{E}$ defined in Eqs. (42). In the field of a single toroidal eigenmode with mode number n, resonant particles on each constant-C surface satisfy an equation analogous to Eq. (61):

$$\ddot{Q} + \omega_{t\ell}^2(C)\sin Q = 0 \qquad \text{with} \qquad Q \equiv n\varphi - \ell\vartheta - \omega t \ . \tag{64}$$

for each value of ℓ (discrete) and C which satisfy the resonance condition $\Omega_\ell = 0$. We remind the reader that ϑ is *not* the poloidal angle but rather the angle conjugate to the unperturbed action

$$I_\vartheta \equiv \frac{1}{2\pi}\oint \mathcal{P}_\theta \, d\theta \ , \tag{65}$$

with $\mathcal{P}_\theta$ the *unperturbed* poloidal momentum. A qualitative diagram of the three-dimensional island structure described by Eq. (64) is shown in Fig. 2. A formula which generalizes Eq. (62) has been developed to describe the saturated state in the TAE problem [33]; this requires an integration over the invariant surfaces $\{C\}$ for each value of ℓ:

$$c^*\,\gamma_L = \frac{\sum_l \int dC\, \omega_{t\ell}^4 \left(\partial F/\partial p\right) / \left(\partial\Omega_\ell/\partial p\right)^3}{\sum_l \int dC\, \omega_{t\ell}^3 \left(\partial F/\partial p\right) / \left(\partial\Omega_\ell/\partial p\right)^3} \ , \tag{66}$$

with c^* a constant analogous to c in Eq. (62). The integrands are to be evaluated at the island centre – that is, at the value of p which gives $\Omega_\ell(C,p) = 0$. Note that $\partial F/\partial p$ in Eq. (66) gives the usual instability drive:

$$\frac{\partial F}{\partial p} = \left.\frac{\partial F}{\partial \mathcal{P}_\varphi}\right|_{\mathcal{E}} + \frac{\omega}{n}\left.\frac{\partial F}{\partial \mathcal{E}}\right|_{\mathcal{P}_\varphi} \ . \tag{67}$$

In Fig. 3 we plot both $\omega_{t\ell}/\gamma_L$ and $\partial F/\partial p$ as functions of C for a passing particle population in an ITER-like plasma. We have attempted to calculate the integrals

in Eq. (66) in order to obtain a value for the constant c^*. Initial estimates show $c^* \sim 5.0$, although the accuracy of this estimate has yet to be established. Finally, we give an example of the island structure on the surface $C = 3.5$ MeV for a small-amplitude perturbation in Fig. 4, in terms of the radial variable $s \equiv [\psi/\psi(a)]^{1/2}$.

When first-order islands associated with different values of ℓ overlap, Eq. (66) breaks down – and in the limit where resonances due to many ℓ values overlap, quasilinear theory becomes applicable.

B. Resonant particle reconstitution

Our kinetic description (see Eq. (46)) is at present somewhat restricted in that we have no physical mechanism to describe the replenishment of resonant particles into the vicinity of a given island. The various ways in which this replenishment takes place have been identified in Ref. 33. These are briefly summarized below.

1. frequency sweeping

If the resonance condition changes adiabatically with time, that is

$$\frac{1}{\omega}\frac{d\omega}{dt} < \frac{\omega_t^2}{\omega}\,, \tag{68}$$

then the (nonlinearly) trapped resonant particles remain trapped in the wave potential, but the island as a whole may change its position in phase spave. A strong local gradient in the distribution f is the result, and may lead to an enhancement in the particle-to-wave power transfer. This effect can be easily reproduced in the present code by prescribing the time dependence of $\omega(t)$.

2. effective particle source

Because of classical electron drag or pitch angle scattering, fast ions can be continuously injected into the resonance region. This injection can be characterized by an *effective reconstitution rate*, $\nu_{\rm eff}$ which is approximately described by a term of the form

$$-\nu_{\rm eff}\,\delta f_{\rm na} \tag{69}$$

added to the RHS of Eq. (46). When the rate $\nu_{\rm eff}$ is much smaller than both $\gamma_{\rm L} - \gamma_{\rm d}$ and $\gamma_{\rm d}$, it can be shown that isolated pulses will occur with the height of each pulse no greater than the level predicted by particle trapping in the absence of the reconstitution. This is the regime that we will consider in our subsequent ITER simulation in Sec. V. When $\gamma_{\rm L}$, $\gamma_{\rm d}$ and $\nu_{\rm eff}$ are comparable, the mode saturation and long-time dynamics become more complicated.

V. Tokamak Simulation

A. Large-aspect-ratio equilibrium

For the examples presented in this paper, we employ a zero-β, large-aspect-ratio equilibrium [23]:

$$\mathbf{B} = \nabla\varphi + \frac{r^2}{q}\nabla\theta \,, \tag{70}$$

This simple equilibrium minimizes initial coding difficulties, enables direct comparison of numerical results with analytic formulae for the linear growth rate, and also provides a convenient benchmark for other numerical codes. The contravariant components of this field – as defined by Eq. (8) – are $g = 1$, $I = r^2/q$ and $\delta = 0$; the poloidal flux is $\chi = r^2/2$, the parallel wavenmber is $k_{\|m} = n - m/q$, and the magnitude of $\mathbf{B}$ is

$$B = \frac{\left(1 + (r/q)^2\right)^{1/2}}{1 + r\cos\theta} \,. \tag{71}$$

The choice of q is arbitrary within the context of this model equilibrium.

B. The thermonuclear alpha distribution

For the equilibrium distribution function we consider a simple product form:

$$f_0 = C\, h_1(\langle\psi\rangle)\, h_2(\mathcal{E}) \,. \tag{72}$$

For anisotropic populations, or when profile effects on the energy dependence are important, Eq. (72) can be generalized accordingly. Presently, we wish to concentrate on a reactor-relevant alpha particle population, in which case the form of h_2 is determined by alpha particle drag arising from collisions with thermal electrons and ions. When reactants (thermal D and T ions) have a common temperature T_i, alpha particles will be produced with a roughly Gaussian-in-energy distribution, as shown by Brysk [34]. This implies an alpha particle source of the form

$$S(v) = S_0 \exp\left[-\frac{(\mathcal{E} - \mathcal{E}_0)^2}{\Delta\mathcal{E}^2}\right] \,, \tag{73}$$

with $\mathcal{E}_0 = 3.6\text{MeV}$ and $\Delta\mathcal{E}[\text{keV}] = 106\sqrt{T_i[\text{keV}]}$. The steady-state distribution of alphas can then be obtained by solving the Fokker-Planck(FP) equation with source, Eq. (73):

$$\tau_s \frac{\partial h_2}{\partial t} = \frac{1}{v^2}\frac{\partial}{\partial v}\left(v^3 + v_c^3\right) h_2 + \tau_s S(v) = 0 \,. \tag{74}$$

The *crossover* velocity, v_c, is given approximately by

$$v_c[\mathrm{cm/s}] \sim 1.7 \times 10^8 \frac{\sqrt{T_e[\mathrm{keV}]}}{(m_i/\mathrm{m_H})^{1/3}} \,. \tag{75}$$

For $\mathcal{E}_0 \gg \Delta\mathcal{E}$, the solution of the FP equation is

$$h_2 = \frac{\mathrm{Erfc}\left[(\mathcal{E} - \mathcal{E}_0)/\Delta\mathcal{E}\right]}{v^3 + v_c^3} \,. \tag{76}$$

We remark that this form gives the correct spread in velocity around the 3.52 MeV birth energy, and for burning plasma, indicates that there can be a substantial number of fast ions produced above the birth energy. Indeed, in a 25 keV plasma, 18% of the alpha particles will have an energy above 4 MeV [35]

The form of h_1 depends sensitively on the plasma temperature and density profiles, and can be calculated directly from these profiles (and also the impurity concentrations). Although plasma density profiles in ITER H-mode are expected to be flat or even hollow, the temperature profile can be quite peaked in the absence of sawtooth activity. In this case a good representation for the radial alpha pressure profile is

$$h_1 = \left(1 - \frac{\langle\psi\rangle}{\psi(a)}\right)^{\alpha} \,, \tag{77}$$

with α an adjustable parameter. However, the appearance of sawteeth are expected to produce a repetitive flattening of the plasma temperature inside the sawtooth mixing radius (roughly $r/a \sim 0.55$). Although we ignore the effect of sawteeth on the alpha orbits, we consider that the plasma temperature profiles can be significantly altered from the peaked pre-sawtooth values. The shape of these flattened profiles can be adequately described by

$$h_1 = \frac{1}{\exp\left(x/\Delta\right) + 1} \,, \tag{78}$$

where $x \equiv \langle\psi\rangle - \psi_0$ and Δ measures the steepness of the alpha gradient at the mixing radius.

C. Code benchmark

We have benchmarked FAC (see discussion following Eq. (53)) in the linear regime against the linear δW code CASTOR-K [36] for identical equilibria and the post-crash-like h_1 profile given by Eq. (78). A value of Δ in accord with expected ITER pressure gradients was used. Also, ψ_0 was taken at the $q = 1$ surface. For the radial

eigenfunction, we use the $n = 10$ core-localized mode shown in Fig. 5. This was computed by the ideal, incompressible MHD code MISHKA1 [37] for a simple equilibrium with circular flux surfaces and q-profile with an extended low-shear region. The two dominant poloidal harmonics, $m = (8, 9)$, are peaked just *inside* the $q = 1$ surface. Our consideration of core-localized-modes is motivated by the important fact that they can be nearly undamped (with regard to continuum damping), and are thus good candidates for TAE instability. Previous analyses have indicated that high-n modes ($10 \lesssim n \lesssim 40$) are the most dangerous for ITER [13-14], while low-n modes are typically stable, since $\omega_{*\alpha} \ll \omega$.

A scan of the linear growth rate versus ω was made with all other parameters kept fixed. Due to the $(\delta f/f_0)^2$ scaling of the particle noise reduction in the noise [38], simulations with very small wave amplitude can very accurately recover the linear growth rate. The agreement between FAC and CASTOR-K results, shown in Fig. 6, is exceptionally good.

D. ITER-like ignited plasma simulation

Our primary goal in an ITER-relevant simulation will be to get a *quantitative* feeling for what saturation amplitudes and levels of anomalous diffusion are possible for strong local instability scenarios. Since we have found that global TAE modes typically suffer strong intrinsic damping (continuum plus radiation) by comparision with core-localized modes, we have restricted our attention to the latter type in this study. It will be necessary for a more conclusive study to consider both local and global modes, as well as drag and pitch angle scattering of the fast ions (as described in Sec. IV.B.). We tentatively expect, however, that the saturated amplitudes calculated in this work will represent an upper-bound to the possible TAE amplitudes one is likely to find in an ITER-like plasma.

Using the MISHKA1 code, we computed a realistic set of weakly-damped, high-n eigenfunctions in the range $17 \leq n \leq 26$. These modes have $m = (n-1, n-2)$, and are thus localized around the $q = (n-3/2)/n$ surface, as shown in Fig. 7. At present, the linear mode computation cannot be automated; rather, it is an extremely laborious procedure. We remark that the q-profile used for the computation of these modes had $q(0) = 0.87$, which is a reasonable value for the pre-sawtooth phase. Also, it was not as flat as for the benchmark. Since the existence of core-localized modes does not require $q(0) < 1$, we expect that simliar modes will exist even when q on axis rises above unity.

Initial linear simulations showed that all such modes are *stable* to (flattened) post-sawtooth crash profiles even in the absence of background (*i.e.*, , thermal electron and ion) damping. This is a consequence of the stabilizing term $\partial f_0/\partial \mathcal{E}$ – which is known to be particularly strong for an isotropic, slowing-down population. Subsequent simulations, however, demonstrated that the same modes are *unstable* to a peaked distribution, Eq. (77), with $\alpha = 4$, since it has a shorter gradient scale length than a post-crash profile inside $q = 1$. We proceeded with this form, using the parameters listed in Table III. First, we ran all modes together in a single simulation with a large value of the fast ion pressure ($\langle \beta_f \rangle = 0.8\%$) and no thermal ion damping.

The time evolution of δB and $\delta\omega$ for each mode is given in Fig. 8, with a superposition of the evolution of every $\delta B/B$ shown in Fig. 9. For the core-localized modes we have computed, CASTOR-K finds that the dominant damping mechanism, ion Landau damping, is roughly $\gamma_d/\omega \sim 2\langle\beta_i\rangle$ for $T_i = 15\,\mathrm{keV}$, where $\langle\beta_i\rangle$ is the volume-averaged thermal ion beta. This result is fairly insensitive to mode structure and small changes in equilibria. For the typical value $\langle\beta_i\rangle \sim 1\%$, then, $\gamma_d/\omega \sim 2\%$. We re-ran the previous simulation including this value of the damping. The result was that growth rates and saturation amplitudes were reduced accordingly, as illustrated in Fig. 10.

Next, we examine the fast particle response to the unstable spectrum. In Fig. 11, the density perturbation as a function of radius and time is plotted. Particles are moved outwards by the unstable modes, and the time-evolved distribution is thus locally flattened. This is consistent with the usual physical picture of the instability; *viz.*, , that the free-energy associated with the unstable distribution in the vicinity of $s \sim 0.3$ is tapped and converted to wave energy. A similar picture – for the density perturbation as a function of energy and time – is given in Fig. 12. The region of velocity resonance is very broad, extending well below 1 MeV, with the strongest interaction in the $3 - 4\,\mathrm{MeV}$ range.

Recent studies indicate that when wave-particle resonance regions overlap, a substantial enhancement of the particle-to-wave energy transfer may occur. The process by which this occurs has been dubbed the *domino effect* [33], according to the way in which adjacent regions of local flattening appear to "topple" onto one another. To quantify such an enhancement in the present case, we calculate the total particle-to-wave energy transfer for all modes, and then rerun the simulation for each of the 10 modes *seperately* and sum the individual energy transfers. The result, shown in Fig. 13, indicates that the power transfer in this case is *not* enhanced by the effect of multiple modes.

Finally, we address the most pressing question regarding the nonlinearly evolved state, namely, the overall anomalous diffusion of the alphas. In Figs. 14 and 15, we, plot the initial and final density of guiding centers; Fig. 14 shows the result for no background damping, and Fig. 15 for 2% ion damping. Clearly, even for the most unstable case – where the growth rates of the modes are likely *far* in excess of expected values – the profile modification is minimal. In fact, the resilience of a machine to diffusion/loss caused by fast-particle instabilities seems to be generally indicated by the size of the parameter Δ_b/a.

It is worth mentioning that we have performed preliminary nonlinear simulations for fishbone modes (the beam-driven $n = 1$ internal kink) in PDX and JET. Experimentally, PDX was observed to lose up to 20% to 40% of perpendicular beam ions; this order has been reproduced self-consistently by FAC. As well, simulation of JET-like plasmas produce large redistribution with negligible losses; again in agreement with experiment. The diffusion for all ITER scenarios we have studied is extremely benign compared with the fishbone-induced losses in these smaller, weak-field machines.

VI. Summary

In this paper a method to calculate the linear growth and nonlinear saturation of Alfvén eigenmodes in general, axisymmetric toroidal geometry has been described. The model has been fully benchmarked with an independent numerical code in the linear regime. The nonlinear evolution of an unstable spectrum of ten core-localized modes – restricted to the radial domain $0.2 \lesssim r/a \lesssim 0.4$ – in a simplified circular geometry was also considered, under otherwise general ITER-like conditions. The simulations indicate that for relevant values of n, such a radially localized group of modes leads to rather insignificant anomalous alpha-particle redistribution even in worse-than-expected conditions. The possibility of significant redistribution via interaction with more radially extended modes (and with the inclusion of collisional effects) is a question that remains the subject of ongoing research.

VII. Acknowledgements

It is with pleasure that the authors thank S.E. Sharapov and S. Pinches for collaboration during research conducted in parallel with the United Kingdom Atomic Energy Authority while one of the authors (J.C.) was a visiting scientist at the JET Joint Undertaking . We are indebted also to T. Hender and L. Appel for their contributions during this collaboration, to members of the Data Analysis and Modeling Division of the JET Joint Undertaking for the hospitality extended during a visit by H.B. during 1995, and to B. Breizman and J.W. Van Dam for discussions during the course of this work. Finally, one of us (J.C.) acknowledges continued financial support from the Natural Sciences and Engineering Research Council of Canada.

This work is supported by the U.S. Department of Energy, Contract No. DE-FG03-96ER-54346.

References

[1] *Technical Basis for the ITER Interim Design Report, Cost Review and Safety Analysis*, ITER EDA Documentation Series No. 7 (International Atomic Energy Agency, Vienna, 1996), p. V-32.

[2] M.N. Rosenbluth and P.H. Rutherford, Phys. Rev. Lett. **34** 1428 (1975).

[3] A.B. Mikhaĭlovskiĭ, Sov. Phys - JETP **41** 890 (1976).

[4] K.L. Wong, R.J. Fonck, S.F. Paul, D.R. Roberts, E.D. Fredrickson, R. Nazikian, H.K. Park, M. Bell, N.L. Bretz, R. Budny, S. Cohen, G.W. Hammett, F.C. Jobes, D.M. Meade, S.S. Medley, D. Mueller, Y. Nagayama, D.K. Owens, and E.J. Synakowski, Phys. Rev. Lett. **66** 1874 (1991).

[5] W.W. Heidbrink, E.J. Strait, E. Doyle, G. Sager, and R.T. Snider, Nucl. Fusion **31** 1635 (1991).

[6] S. Ali-Arshad and D.J. Campbell, Plasma Phys. and Contr. Fusion **36** 879 (1994).

[7] A. Fasoli, D. Borba, G. Bosia, D.J. Campbell, J.A. Dobbing, C. Gormezano, J. Jacquinot, P. Lavanchy, P. Marmillod, A. Santagiustina, and S. Sharapov, Phys. Rev. Lett. **75** 645 (1995).

[8] R. Nazikian, G.Y. Fu, S.H. Batha, M.G. Bell, R.V. Budny, C.E. Bush, Z. Chang, Y. Chen, C.Z. Cheng, D.S. Darrow, P.C. Efthimion, E.D. Fredrickson, N.N. Gorelenkov, B. Leblanc, F.M. Levinton, R. Majeski, E. Mazzucato, S.S. Medley, H.K. Park, M.P. Petrov, D.A. Spong, J.D. Strachan, E.J. Synakowski, G. Taylor, S. Von Goeler, R.B. White, K.L. Wong, and S.J. Zweben, submitted to Phys. Rev. Lett.

[9] G.Y. Fu and C.Z. Cheng, Phys. Fluids B **4** 3722 (1992).

[10] G.Y. Fu and C.Z. Cheng, Phys. Fluids B **5** 4040 (1993).

[11] J. Candy and M.N. Rosenbluth, Nucl. Fusion **35** 1069 (1995).

[12] J. Candy, Plasma Phys. and Contr. Fusion **38** 795 (1996).

[13] J. Candy, Ph.D. thesis, University of California, San Diego, (1994).

[14] S. Putvinski, H. Berk, P. Barabaschi, B.N. Breizman, D. Borba, J. Candy, C.Z. Cheng, B. Coppi, N. Doinikov, G.Y. Fu, R.J. Hastie, G.T.A. Huysmans, W. Kerner, S.V. Konovalov, S. Migliuolo, F. Porcelli, F. Romanelli, M.N. Rosenbluth, S.E. Sharapov, K. Tani, K. Tobita, B. Tubbing, J. Van Dam, R.B. White, Y. Wu, P.N. Yushmanov, L.E. Zakharov, F. Zonca, and S.J. Zweben, in *Plasma Physics and Controlled Nuclear Fusion Research 1994* (Proc. 15th Int. Conf. Seville, Spain, 1994), Vol. 2, IAEA, Vienna 535 (1996).

[15] H.L. Berk, B.N. Breizman and M. Pekker, in *Physics of High Energy Particles in Toroidal Systems* (AIP Conf. Proc. 311, T. Tajima and M. Okamoto, eds), AIP, New York 18 (1994).

[16] H.L. Berk, B.N. Breizman and M. Pekker, Phys. Plasmas **2** 3007 (1995).

[17] B.N. Breizman, H.L. Berk, M.S. Pekker, F. Porcelli, G.V. Stupakov, and K.L. Wong, "Critical nonlinear phenomena for kinetic instabilities near threshold," submitted to Phys. Plasmas.

[18] Y. Wu and R.B. White, Phys. Plasmas **1** 2733 (1994).

[19] Y. Wu, R.B. White, Y. Chen and M.N. Rosenbluth, Phys. Plasmas **5** 1200 (1995).

[20] G.Y. Fu and W. Park, Phys. Rev. Lett. **74** 1594 (1995).

[21] D. Borba, J. Candy, H. Holties, G. Huysmans, W. Kerner, and S. Sharapov, in *Proceedings of the 22nd EPS Conference on Controlled Fusion and Plasma Physics* (Bournemouth, U.K.), Vol 19C II 237 (1995).

[22] L. Chen, Phys. Plasmas **1** (1994) 1519; also S. Briguglio, C. Kar, F. Romanelli, G. Vlad and F. Zonca, Plasma Phys. and Contr. Fusion **37** A279 (1995).

[23] R.B. White and M.S. Chance, Phys. Fluids **27** (1984) 2455.

[24] B.N. Breizman and S.E. Sharapov, Plasma Phys. and Contr. Fusion **37** 1057 (1995).

[25] H.L. Berk, B.N. Breizman and H. Ye, Phys. Fluids B **5** 1506 (1993).

[26] J. Candy, J. Comput. Phys. **129** 160 (1996).

[27] F. Porcelli, R. Stankiewicz, W. Kerner and H.L. Berk, Phys. Plasmas **1** 470 (1994).

[28] L. Chen, R.B. White and M.N. Rosenbluth, Phys. Rev. Lett. **52** 1122 (1984).

[29] T.H. Stix, Nucl. Fusion **15** 737 (1975).

[30] I.B. Bernstein, S.K. Trehan, and M.P.H. Weenink, Nucl. Fusion **4** 61 (1964).

[31] B.V. Chirikov, Phys. Reports **52** 263 (1979).

[32] M.B. Levin, M.G. Lyubarsky, I.N. Onishchenko, V.D. Shapiro, and V.I. Shevchenko, Sov. Phys - JETP **35** 898 (1972).

[33] H.L. Berk, B.N. Breizman, J. Fitzpatrick, M.S. Pekker, H.V. Wong, and K.L. Wong, Phys. Plasmas **3** 1827 (1996).

[34] H. Brysk, Plasma Phys. **15** 611 (1973).

[35] G. Sadler and P. van Belle, in *Proceedings of the 22nd EPS Conference on Controlled Fusion and Plasma Physics, 1995* (Bournemouth, U.K.), Vol 19C II 269 (1995).

[36] D. Borba, J. Candy, A. Fasoli, W. Kerner, D. Muir, and S. Sharapov, *Joint European Torus Report JET-P(96)30*, July 1996.

[37] A.B. Mikhaĭlovskiĭ, G.T.A. Huysmans, W.O.K. Kerner, and S.E. Sharapov, *Joint European Torus Report JET-P(96)25*, July 1996.

[38] G. Hu and J.A. Krommes, Phys. Plasmas **1**, 863 (1994).

[39] T. Fülöp, M. Lisak, Ya. I. Kolesnichenko, and D. Anderson, Plasma Phys. and Contr. Fusion **38** 811 (1996).

Appendix A: Terms in Equations of Motion

The partial derivatives of the electrostatic potential which appear in the guiding-center equations take the form

$$\Phi_{\psi j} \equiv \frac{\partial \Phi_j}{\partial \psi_j} = \sum_{k=1}^{n_w} \sum_{m=m_k^-}^{m_k^+} \left[\mathcal{X}_k \cos\Theta_{jkm} \frac{\partial \phi_{km}(\psi_j)}{\partial \psi_j} + \mathcal{Y}_k \sin\Theta_{jkm} \frac{\partial \phi_{km}(\psi_j)}{\partial \psi_j} \right] \quad (A1)$$

$$\Phi_{\varphi j} \equiv \frac{\partial \Phi_j}{\partial \varphi_j} = -\sum_{k=1}^{n_w} \sum_{m=m_k^-}^{m_k^+} \left[\mathcal{X}_k \sin\Theta_{jkm} - \mathcal{Y}_k \cos\Theta_{jkm} \right] n_k \phi_{km}(\psi_j) \ , \quad (A2)$$

$$\Phi_{\theta j} \equiv \frac{\partial \Phi_j}{\partial \theta_j} = \sum_{k=1}^{n_w} \sum_{m=m_k^-}^{m_k^+} \left[\mathcal{X}_k \sin\Theta_{jkm} - \mathcal{Y}_k \cos\Theta_{jkm} \right] m \phi_{km}(\psi_j) \ , \quad (A3)$$

$$\Phi_{tj} \equiv \frac{\partial \Phi_j}{\partial t} = \sum_{k=1}^{n_w} \sum_{m=m_k^-}^{m_k^+} \Big[\dot{\mathcal{X}}_k \cos\Theta_{jkm} + \dot{\mathcal{Y}}_k \sin\Theta_{jkm}$$
$$+ \omega_k (\mathcal{X}_k \sin\Theta_{jkm} - \mathcal{Y}_k \cos\Theta_{jkm}) \Big] \phi_{km}(\psi_j) \ . \quad (A4)$$

Next, derivatives of the function α can be expressed as

$$\alpha_{\psi j} \equiv B_j \frac{\partial \alpha_j}{\partial \psi_j}$$
$$= \sum_{k=1}^{n_w} \sum_{m=m_k^-}^{m_k^+} \frac{k_{\parallel m}}{\omega_k} \left[\left(\mathcal{X}_k \cos\Theta_{jkm} \frac{\partial \phi_{km}(\psi_j)}{\partial \psi_j} + \mathcal{Y}_k \sin\Theta_{jkm} \frac{\partial \phi_{km}(\psi_j)}{\partial \psi_j} \right) \right.$$
$$- \frac{1}{B_j} \frac{\partial B_j}{\partial \psi_j} (\mathcal{X}_k \cos\Theta_{jkm} + \mathcal{Y}_k \sin\Theta_{jkm}) \phi_{km}(\psi_j)$$
$$\left. + \frac{m}{k_{\parallel m} q_j^2} \frac{dq_j}{d\psi_j} (\mathcal{X}_k \cos\Theta_{jkm} + \mathcal{Y}_k \sin\Theta_{jkm}) \phi_{km}(\psi_j) \right] \ , \quad (A5)$$

$$\alpha_{\varphi j} \equiv B_j \frac{\partial \alpha_j}{\partial \varphi_j}$$
$$= -\sum_{k=1}^{n_w} \sum_{m=m_k^-}^{m_k^+} \frac{k_{\parallel m}}{\omega_k} \left[\mathcal{X}_k \sin\Theta_{jkm} - \mathcal{Y}_k \cos\Theta_{jkm} \right] n_k \phi_{km}(\psi_j) \ , \quad (A6)$$

$$\alpha_{\theta j} \equiv B_j \frac{\partial \alpha_j}{\partial \theta_j}$$

$$= \sum_{k=1}^{n_w} \sum_{m=m_k^-}^{m_k^+} \frac{k_{\|m}}{\omega_k} \left[m(\mathcal{X}_k \sin\Theta_{jkm} - \mathcal{Y}_k \cos\Theta_{jkm}) \right.$$

$$\left. - \frac{1}{B_j} \frac{\partial B_j}{\partial \theta_j} (\mathcal{X}_k \cos\Theta_{jkm} + \mathcal{Y}_k \sin\Theta_{jkm}) \right] \phi_{km}(\psi_j) \ , \qquad (A7)$$

$$\alpha_{tj} \equiv B_j \frac{\partial \alpha_j}{\partial t}$$

$$= \sum_{k=1}^{n_w} \sum_{m=m_k^-}^{m_k^+} \frac{k_{\|m}}{\omega_k} \left[\dot{\mathcal{X}}_k \cos\Theta_{jkm} + \dot{\mathcal{Y}}_k \sin\Theta_{jkm} \right.$$

$$\left. + \omega_k (\mathcal{X}_k \sin\Theta_{jkm} - \mathcal{Y}_k \cos\Theta_{jkm}) \right] \phi_{km}(\psi_j) \ , \qquad (A8)$$

The partial time derivatives of ϕ and α, given in Eqs. (A4) and (A8), are required to compute the time derivative of $H_{\rm gc}$:

$$\dot{H}_{\rm gc} = -v_{\|j} \alpha_{tj} + \Phi_{tj} \ . \qquad (A9)$$

Appendix B: Linear Growth Rate

For a preliminary validation of the code, we must choose some relevant limiting case for which analytic results can be obtained, and then reproduce these results numerically. A particularly simple regime is the large-aspect-ratio, large field (*i.e.*, thin orbit) limit — for which it is straightforward to calculate an analytic expression for the linear growth rate. We begin with a single-helicity perturbation,

$$\Phi = \mathcal{X}(t) e^{i(n\varphi - m\theta - \omega t)} \phi_m(r) \; . \tag{B1}$$

This this form results in no loss of generality should be evident. Also, the radial part ϕ_m may be arbitrarily broad; that is, we shall make no assumptions regarding radial localization of the mode. In the interest of simplicity, we have fixed the wave phase by directly setting $\mathcal{Y} = 0$. This neglects the small frequency shift which occurs in the presence of a perturbation.

The derivation of the growth rate is exceptionally simple if one considers f_0 to depend on the *perturbed* constants of motion — in contrast to the formal structure of the numerical model. Since the perturbation can be taken to be arbitrarily small, the result for the linear growth is unaffected. Using Eqs. (18a) and (A9) to obtain the rate of change of energy and canonical momentum, respectively, we can write the fast-particle kinetic equation as

$$\frac{d\delta f}{dt} = i \left(\omega - k_{\parallel m} v_\parallel\right) \left(f_\mathcal{E} + \frac{n}{\omega} f_P\right) \Phi \; , \tag{B2}$$

with

$$f_\mathcal{E} \equiv \frac{\partial f_0}{\partial \mathcal{E}} \qquad \text{and} \qquad f_P \equiv \frac{\partial f_0}{\partial \mathcal{P}_\varphi} \; . \tag{B3}$$

We remark that the time derivative operator, when applied to the perturbation Φ, becomes.

$$\frac{d}{dt} = -i \left(\omega - k_{\parallel m} v_\parallel\right) + \mathbf{v}_D \cdot \nabla \; . \tag{B4}$$

The first term on the RHS of Eq. (B4) refers to the zero-order field line motion, which will define our integration characteristics, while the second gives the deviation from this motion. In a strong magnetic field, the latter, or "drift", motion is much slower than the former. A formal integration of the kinetic equation, along with a substitution using Eq. (B4), gives

$$\delta f(t) = \left(f_\mathcal{E} + \frac{n}{\omega} f_P\right) \int_{-\infty}^{t} d\tau \left(-\frac{d}{d\tau} + \mathbf{v}_D \cdot \nabla\right) \Phi \; . \tag{B5}$$

Now, the term associated with the total time derivative in the integrand gives the adiabatic particle response. This does not contribute to the wave growth and is subsequently ignored. The task at hand, then, is too calculate an explicit expression for the drift velocity $\mathbf{v}_D$ in the equilibrium given by Eq. (69). For simplicity, a beam-like population of particles is considered (case (i)), for which $\mu = 0$ and $v_\parallel$ is constant. An inspection of the equations of motion reveals the fast and slow timescales (expressed in terms of unnormalized variables)

$$\omega_c \tau_0 = \frac{\omega_c R_0}{v_\parallel} \qquad \text{and} \qquad \omega_c \tau_1 = \left(\frac{\omega_c R_0}{v_\parallel}\right)^2 \frac{r}{R_0}, \frac{\omega_c R_0}{v_\parallel}\frac{R_0}{r} \; . \tag{B6}$$

Expanding Eqs. (18c,d) and (21) according to this ordering, we find for the fast motion: $\dot{r}_0 = 0$, $\dot{\theta}_0 = v_\parallel/q$ and $\dot{\varphi}_0 = v_\parallel$. Some algebra then gives the slow terms as

$$\dot{r}_1 = -v_\parallel^2 \sin\theta \tag{B7a}$$

$$r\dot{\theta}_1 = -\left(v_\parallel^2 + \frac{\dot{r}^2}{q} v_\parallel\right)\cos\theta \tag{B7b}$$

$$\dot{\varphi}_1 = -v_\parallel r^2 \cos\theta \tag{B7c}$$

These results for the drift velocity imply

$$\mathbf{v}_D \cdot \nabla\Phi = -v_\parallel^2 \left[\sin\theta \frac{\partial\Phi}{\partial r} - i\cos\theta\left(\frac{m}{r} + \frac{k_\parallel m r}{v_\parallel}\right)\Phi\right] \; . \tag{B8}$$

Concentrating on the resonance $\omega - k_{\parallel(m-1)} v_\parallel = 0$ (which will be relevant for co-passing particles), we then evaluate the integral in Eq. (B5) along the unperturbed trajectories $\varphi_0(\tau) = v_\parallel \tau$, $\theta_0(\tau) = v_\parallel \tau/q$ at constant radius to find

$$\delta f(\varphi, \theta, r, v_\parallel, t) = g(r, v_\parallel)\mathcal{X}(t) e^{i(n\varphi - (m-1)\theta - \omega t)} \; , \tag{B9}$$

where

$$g = -\frac{i\pi}{2} v_\parallel^2 \left(f_\mathcal{E} + \frac{n}{\omega} f_P\right)\left[\frac{d\phi_m}{dr} + \left(\frac{m}{r} - \frac{k_\parallel m r}{v_\parallel}\right)\phi_m\right]\delta\left(k_{\parallel(m-1)} v_\parallel - \omega\right) \; . \tag{B10}$$

For the amplitude evolution, we use the continuous version of Eq. (51a):

$$\dot{\mathcal{X}} = -\frac{1}{2E}\int d\Gamma^{(p)}\, \delta f \, \left(\omega - k_{\parallel m} v_\parallel\right) \sin(n\varphi - m\theta - \omega t)\, \phi_m \; . \tag{B11}$$

Integrating by parts and once again ignoring the reactive contribution gives a final expression for the fractional growth rate γ_L/ω:

$$\frac{\gamma_L}{\omega} = \frac{\pi^4}{2E\omega^2} \int_0^a r\,dr\,u^7 \left(f_\varepsilon + \frac{n}{\omega} f_P\right) \left[\frac{d\phi_m}{dr} + \left(\frac{m}{r} - \frac{k_{\parallel m} r}{v_\parallel}\right) \phi_m\right]^2 , \qquad (B12)$$

with $u = \omega / k_{\parallel(m-1)}(r)$. In this result, the distribution is evaluated at the resonant velocity $v_\parallel = u$. Finally, writing f_0 as a function of the averaged poloidal flux $\langle\psi\rangle$ as defined by Eq. (57) of Section 3.2, we can transform back to the $(\psi, \mathcal{E})$ representation according to

$$f_\varepsilon + \frac{n}{\omega} f_P \to \frac{\partial F}{\partial \mathcal{E}} - \frac{m-1}{q\omega} \frac{\partial F}{\partial \psi} . \qquad (B13)$$

This result illustrates clearly a point which is the source of some confusion, and has been mentioned recently in a paper by Fülöp *et al.* [39]. Fundamental considerations show that the instability drive (through f_P) is proportional to the toroidal mode number n. However, calculations in the ZOW limit have shown that the drive scales with the poloidal mode number m rather then n. The difference is explained by the dependence of $\mathcal{P}_\varphi$ on the particle energy. This effect, when combined with the evaluation of $v_\parallel$ at the resonant velocity $\omega / k_{\parallel(m-1)}(r)$, gives a scaling of the drive term with m rather than n.

Table I
Simulation Units

Dimension	Unit	Description
mass	m	fast-particle mass
length	R_0	major radius
time	$1/\omega_c$	inverse, on-axis gyrofrequency
magnetic field	B_0	on-axis magnetic field

Table II
Volume Elements

$d\mathcal{U}$	$dv\, d\lambda\, d\psi\, d\varphi\, d\theta$
$d\Gamma$	$2\pi\mu\, dP_\varphi\, dP_\theta\, d\varphi\, d\theta$
$d\Gamma^{(p)}$	$2\pi v^2\, dv\, d\lambda\, \mathcal{J}\, d\psi\, d\varphi\, d\theta$
$\mathcal{M}$	$2\pi\, v^2 D/B^2$
$\mathcal{N}$	$\mathcal{J}B^2/D$

Table III
ITER Transport Simulation

n_i	6×10^{13}cm^3
m_i/m_H	2.5 (D-T)
a	280 cm
R_0	800 cm
B_0	5.8 T
T_e	15 keV
T_i	15 keV
m_f/m_H	4 (α)
$\langle\beta_f\rangle$	0.8 %

Figure Captions

[1] High-n linear instability window for TAE modes in an ITER-like plasma, calculated using a large-aspect-ratio, boundary layer code. The background damping is the sum of electron and ion Landau damping, collisional electron damping, and radiative/continuum damping.

[2] Illustration of the wave-particle resonant island structure as a function of C, which labels the continuum of Poincaré surfaces-of-section, and p, which labels successive contours on each surface. The phase variable is $Q \equiv n\varphi - \ell\theta - \omega t$.

[3] Variation of the trapping frequency (solid line) and instability drive (dashed line) for a range of surface levels, C, in an ITER-like plasma. The passing particle resonance ($\mu = 0$) is driven by an $\ell = 9$ island resulting from the $(n, m) = (10, 10)$ component of a core localized mode with saturated amplitude $\delta B/B = 4 \times 10^{-5}$. The instability drive has been averaged to yield the unperturbed value.

[4] The $\ell = 9$ island structure on the surface $C = 3.5$ MeV. The parameters are the same as in Fig. 4, but the amplitude of the eigenmode has been increased to $\delta B/B = 3.25 \times 10^{-4}$.

[5] Plot of the $m = (8, 9)$ poloidal harmonics for an $n = 10$ core-localized-mode in an ITER-like circular equilibrium. All other harmonics are negligible.

[6] Benchmark linear growth rate comparsion between the nonlinear FAC code and the linear CASTOR-K code for the mode shown in Fig. 1. Identical circular equilibria are used. Considering that there are differences in the method used to compute equilibrium orbit averages (see Eq. (51)), the agreement is excellent.

[7] Upper core-localized TAE modes in the $m = (n - 1, n - 2)$ gap.

[8] Plots of $\delta B/B$ (smooth curves; log scale with range $10^{-6} \leq \delta B/B \leq 2 \times 10^{-3}$) and $\delta\omega/\omega$ (noisy curves; linear scale with range $-0.2 \leq \delta\omega/\omega \leq 0.2$) for each toroidal eigenmode. In this case the modes are interacting and there is no background wave damping.

[9] Superposition of the time evolution of $\delta B/B$ for the modes shown in Fig. 8.

[10] Same as Fig. 9, except with background ion Landau damping $\gamma_d/\omega = 2\%$ for each mode. This value, sensitive only to ion temperature, is characteristic for plasmas with $T_i = 15$ keV at the TAE location.

[11] Time evolution of the fast ion density perturbation as a function of radius. This was obtained by numerical integration of δf_{na} over all degrees of freedom except radius.

[12] Time evolution of the fast ion density perturbation as a function of energy, which shows strong interaction beyond 3.5 MeV.

[13] A comparison of the total particle-to-wave energy transfer as a function of time. The solid curve is the result for interacting modes (see Fig. 9), while the dotted curve was computed by simulating each mode individually. In this case, a collective enhancement of the energy transfer does *not* occur.

[14] The self-consistent anomalous alpha diffusion caused by the strong instability scenario for 10 upper-core-localized TAE. The vertical dotted lines correspond to those in Fig. 7. Diffusion is rather small and well-localized to the region containing the eigenfunctions, even though the most unstable mode had a growth rate $\gamma_L/\omega \sim 8\%$ – which is at least one order of magnitude above expected values.

[15] Same as in Fig. 14, but with $\gamma_d/\omega = 2\%$.

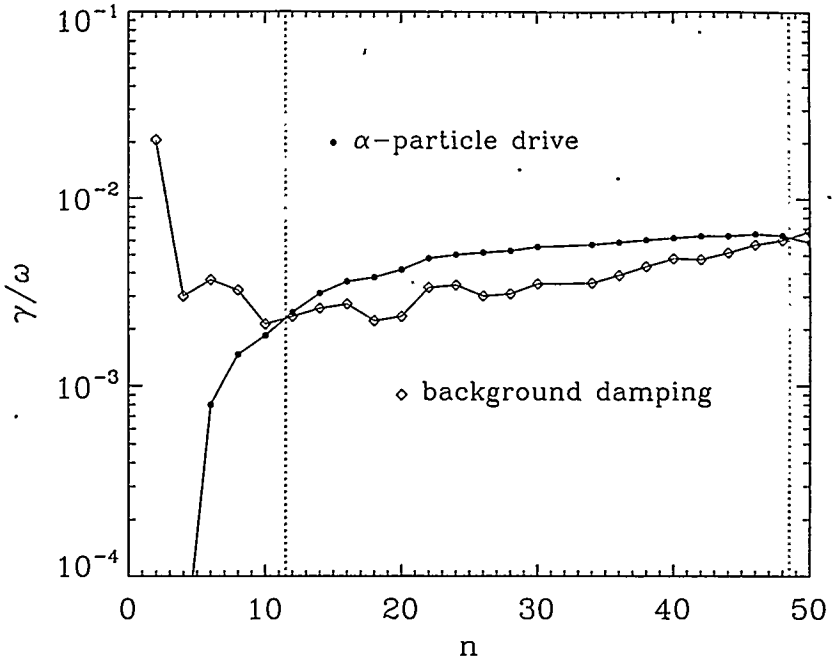
10^{-1}
10^{-2}
10^{-3}
10^{-4}
γ/ω
• α−particle drive
◇ background damping
0
10
20
30
40
50
n

FIG. 1. Candy

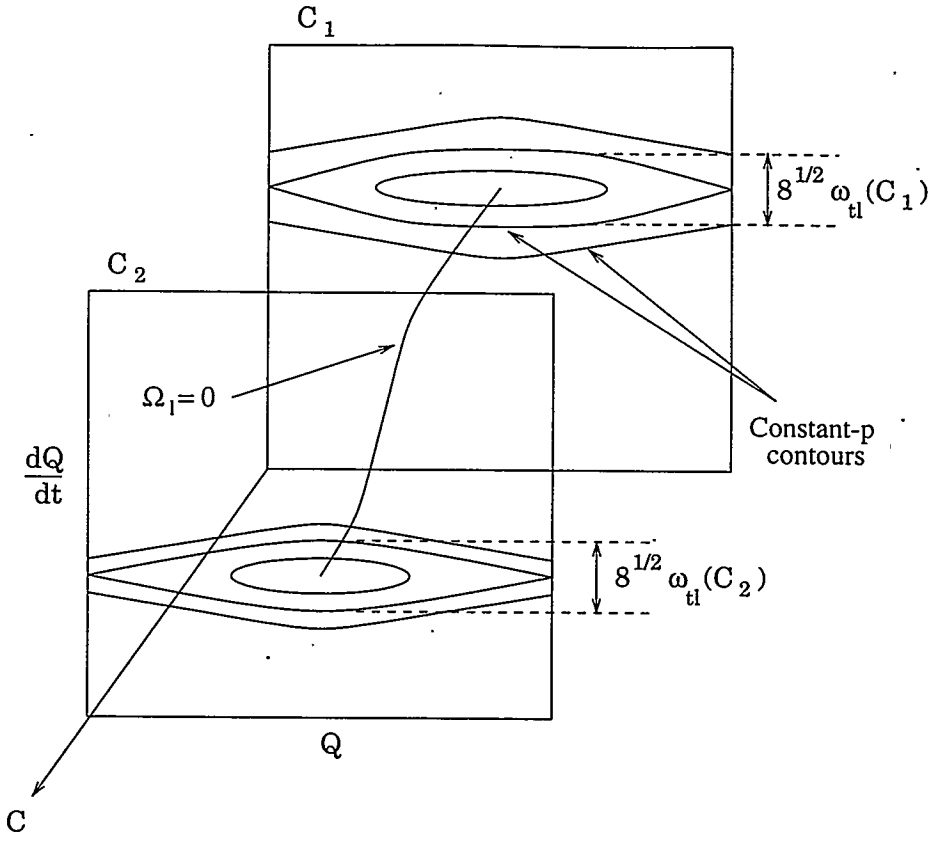

FIG. 2. Candy

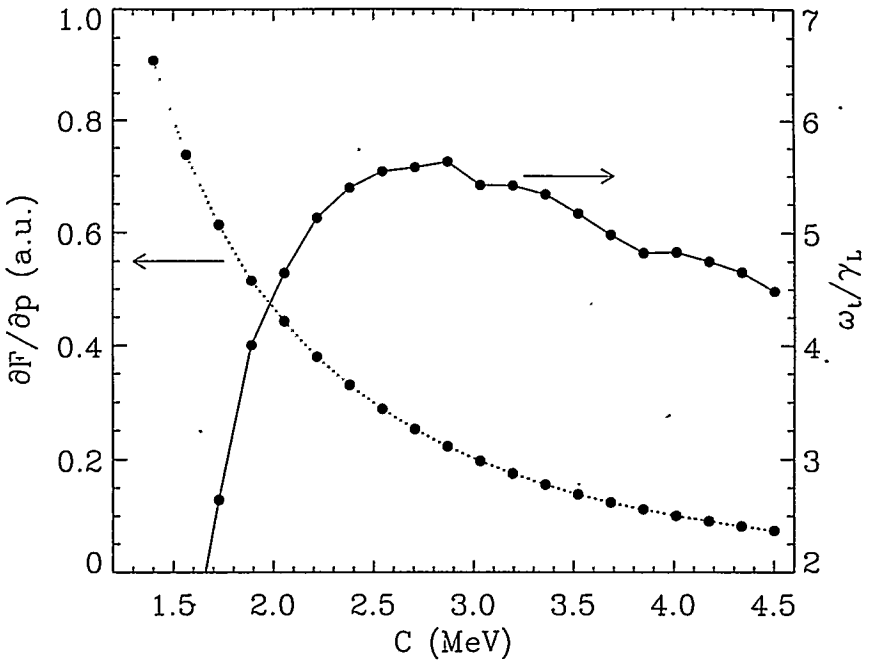

FIG. 3. Candy

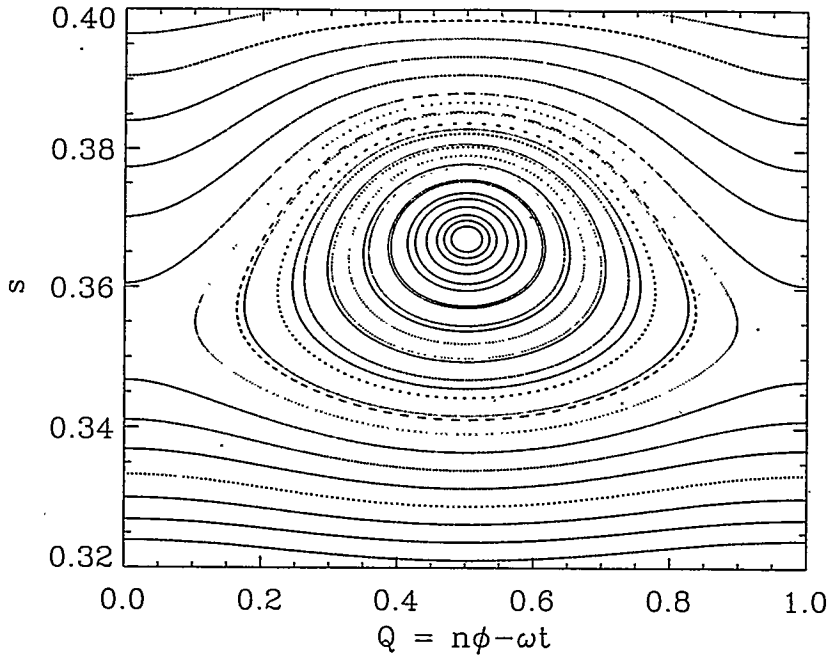

FIG. 4. Candy

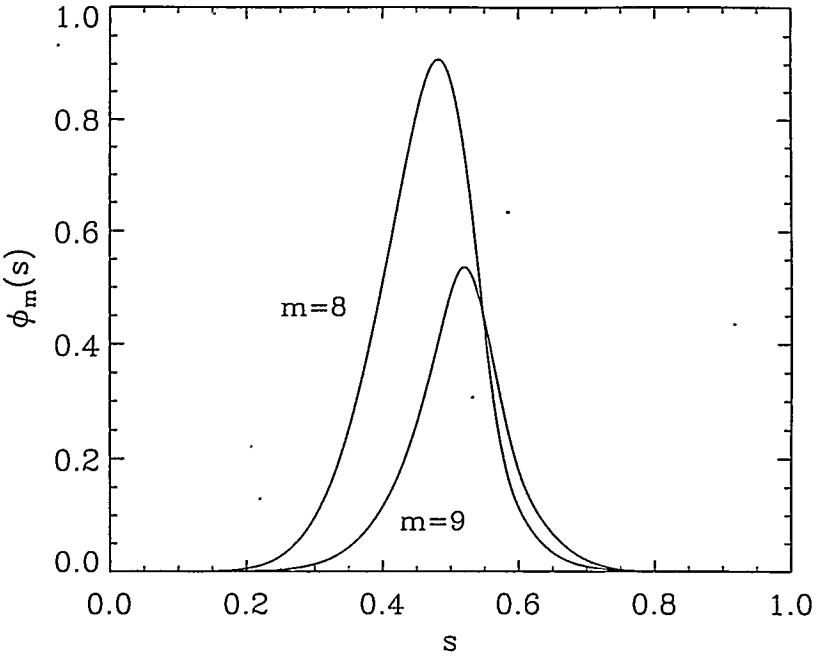

FIG. 5. Candy

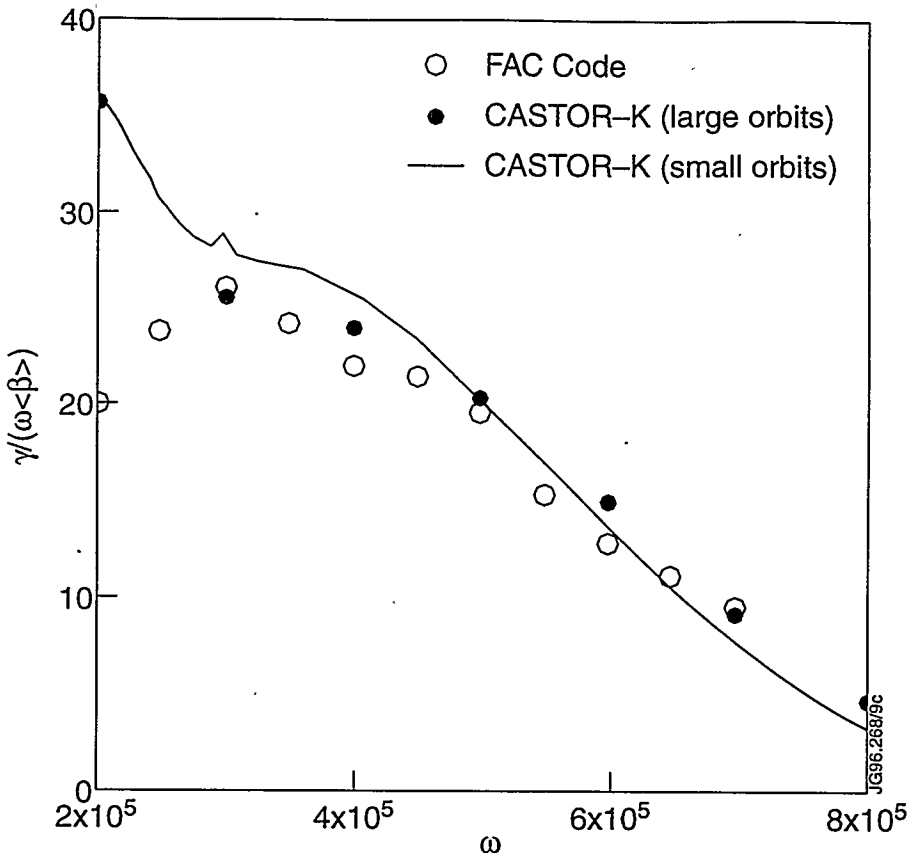
FAC Code
CASTOR–K (large orbits)
CASTOR–K (small orbits)
40
30
20
10
0
γ/(ω<β>)
2x10^5
4x10^5
6x10^5
8x10^5
ω
JG96.268/9c

FIG. 6. Candy

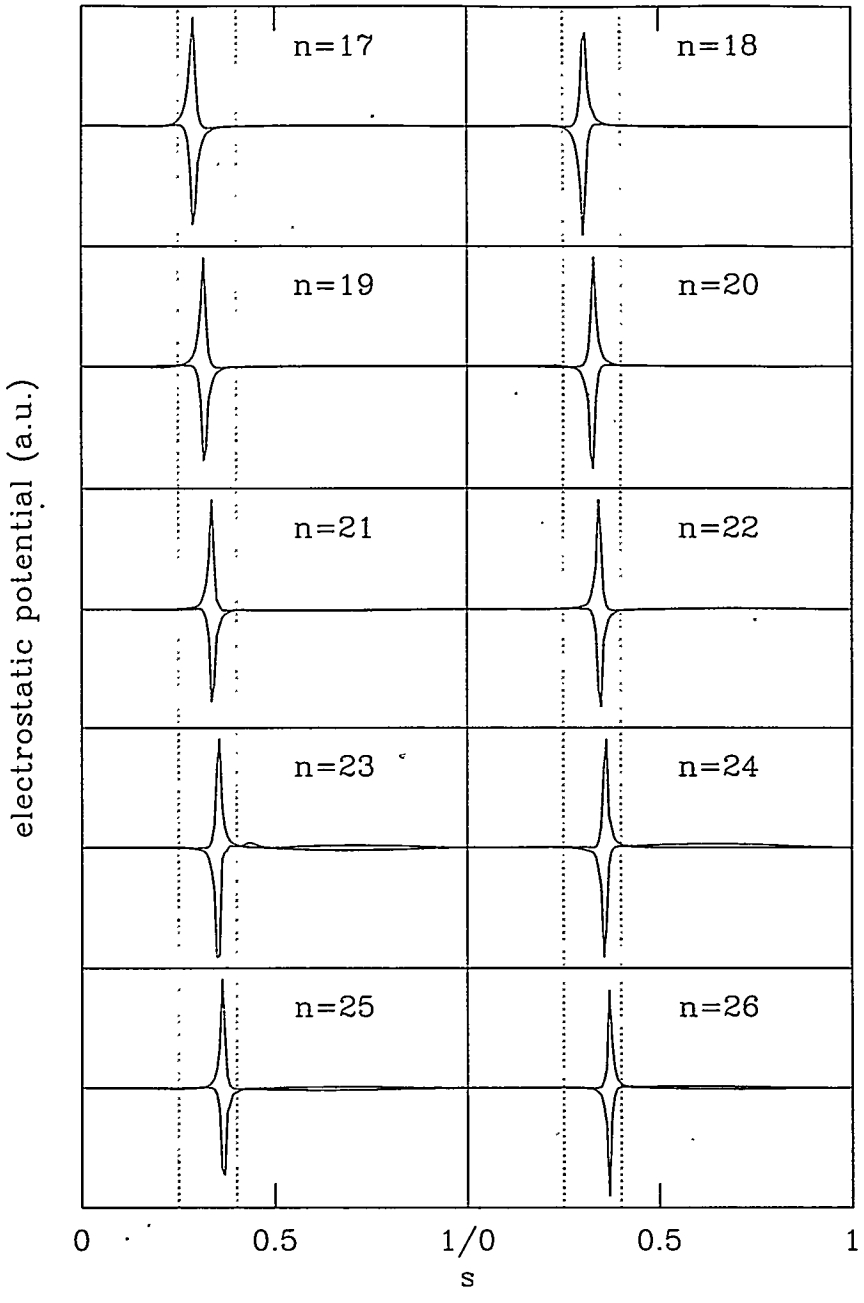
n=17
n=18
n=19
n=20
n=21
n=22
n=23
n=24
n=25
n=26
electrostatic potential (a.u.)
0
0.5
1/0
0.5
1
s

FIG. 7. Candy

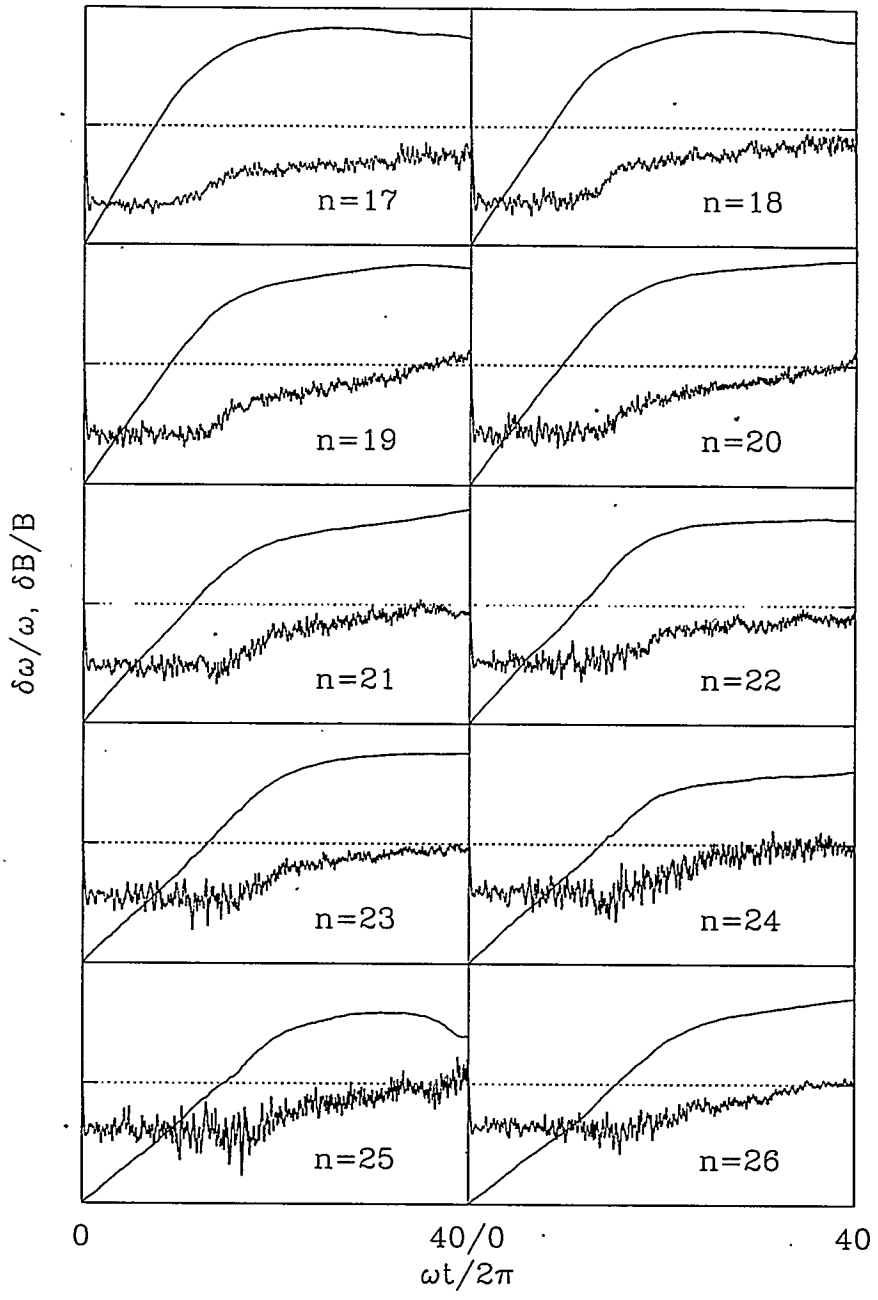

FIG. 8. Candy

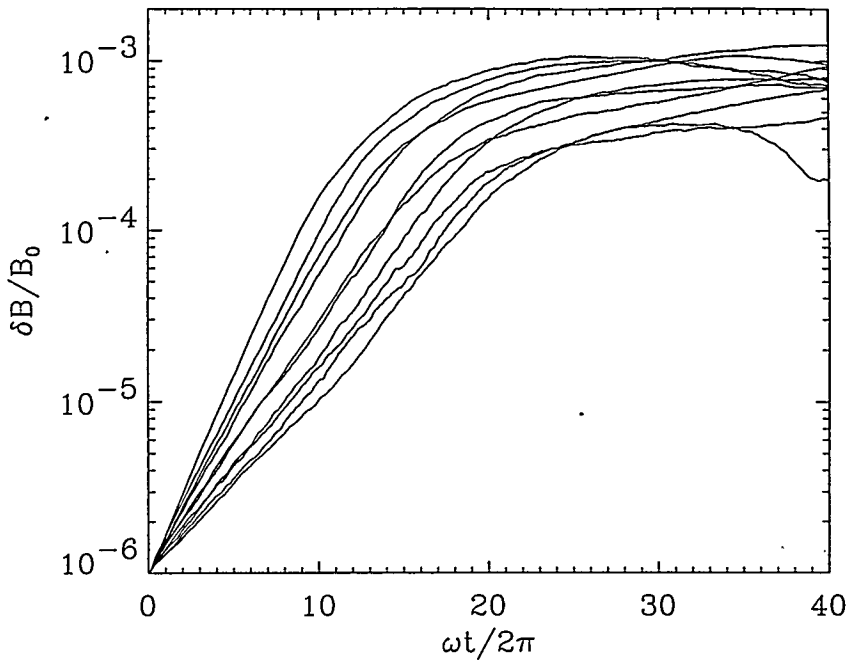

FIG. 9. Candy

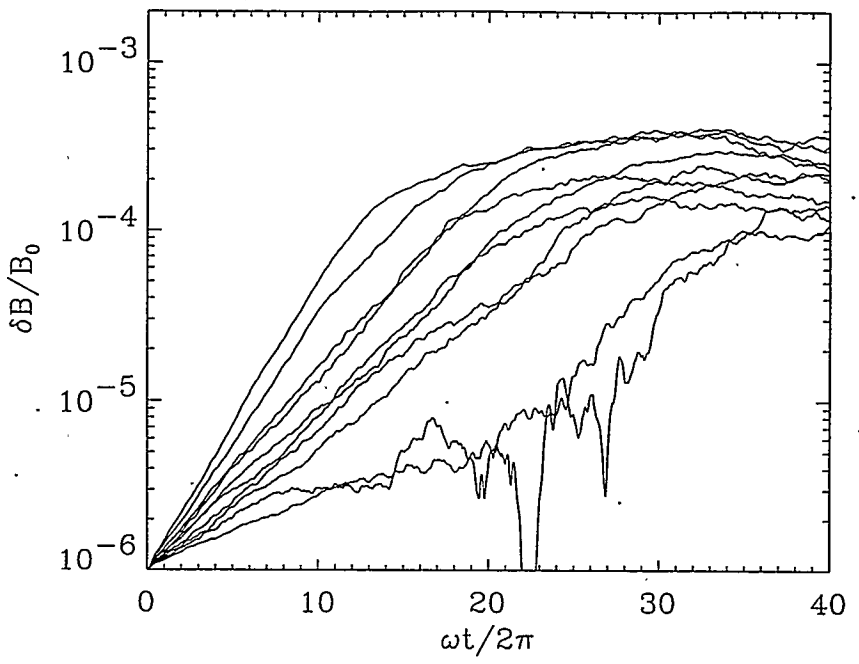

FIG. 10. Candy

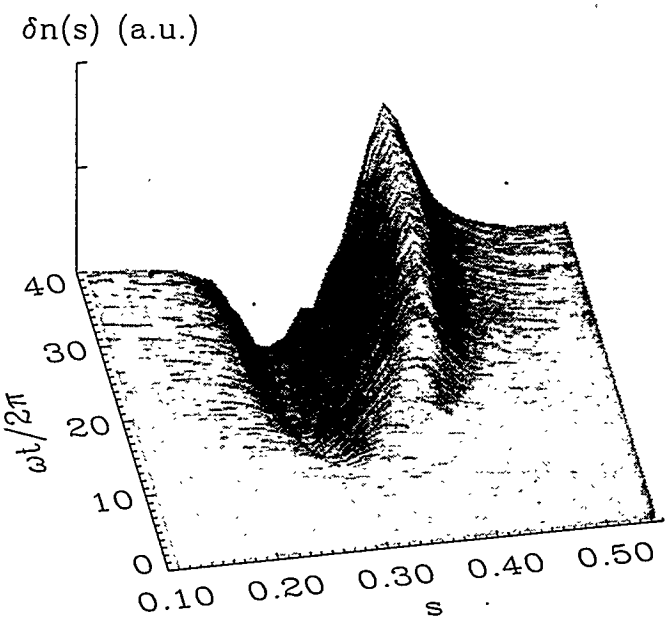

FIG. 11. Candy

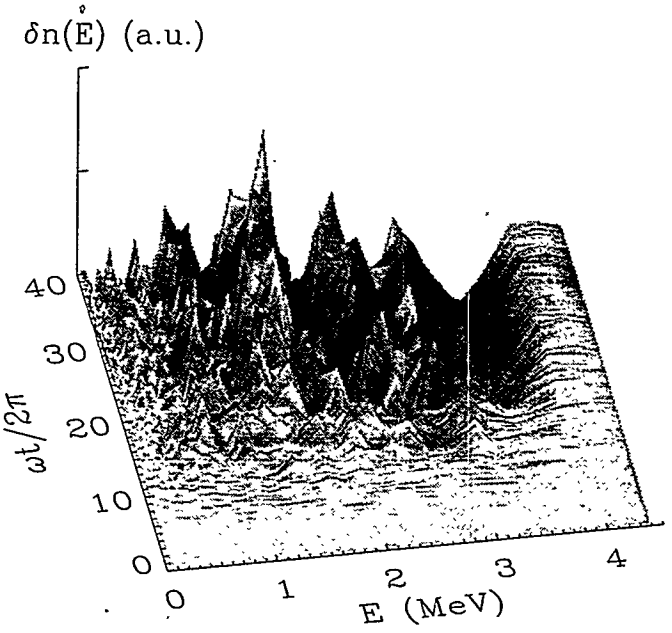

FIG. 12. Candy

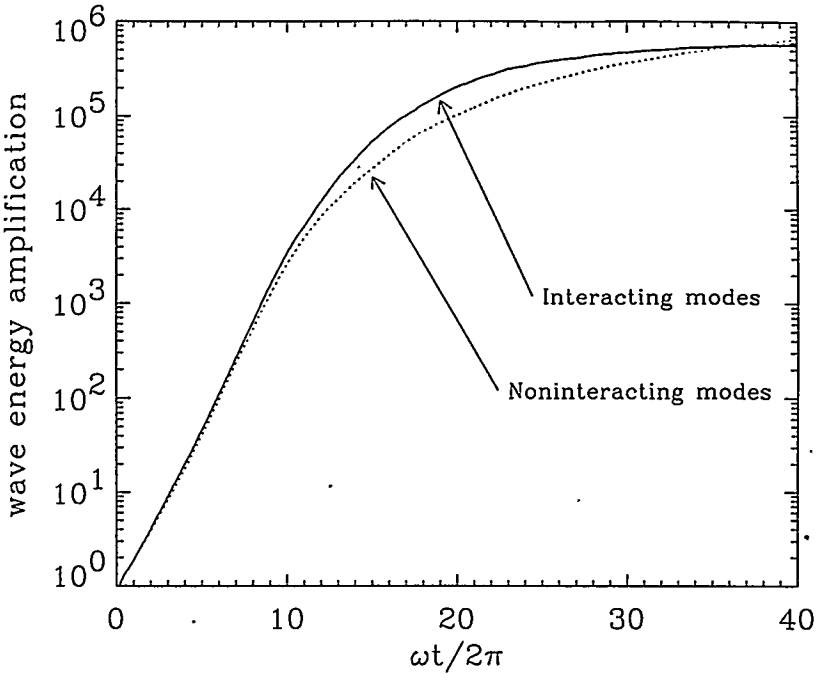
wave energy amplification
10^6
10^5
10^4
10^3
10^2
10^1
10^0
0
10
20
30
40
$\omega t/2\pi$
Interacting modes
Noninteracting modes

FIG. 13. Candy

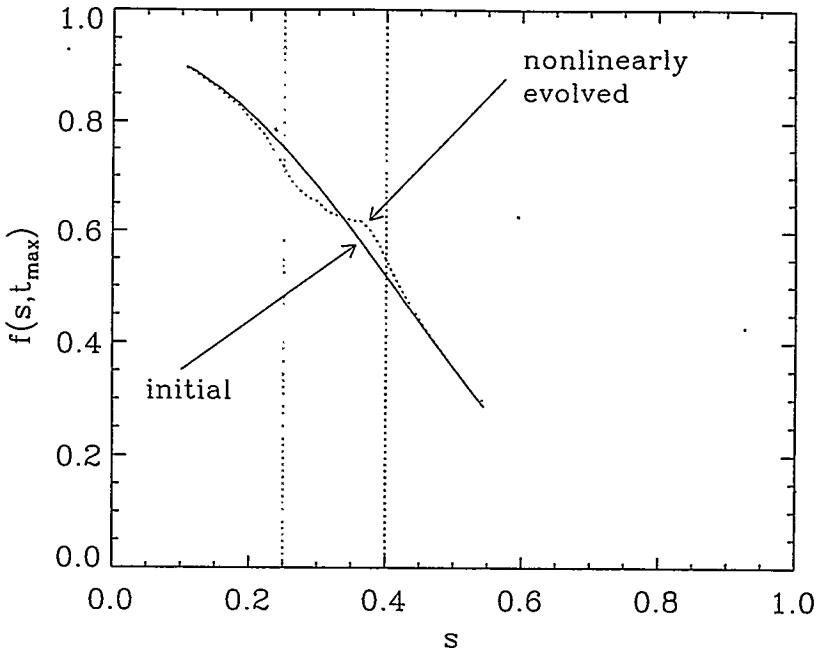
1.0
0.8
0.6
0.4
0.2
0.0
f(s,t_max)
0.0
0.2
0.4
0.6
0.8
1.0
s
nonlinearly
evolved
initial

FIG. 14. Candy

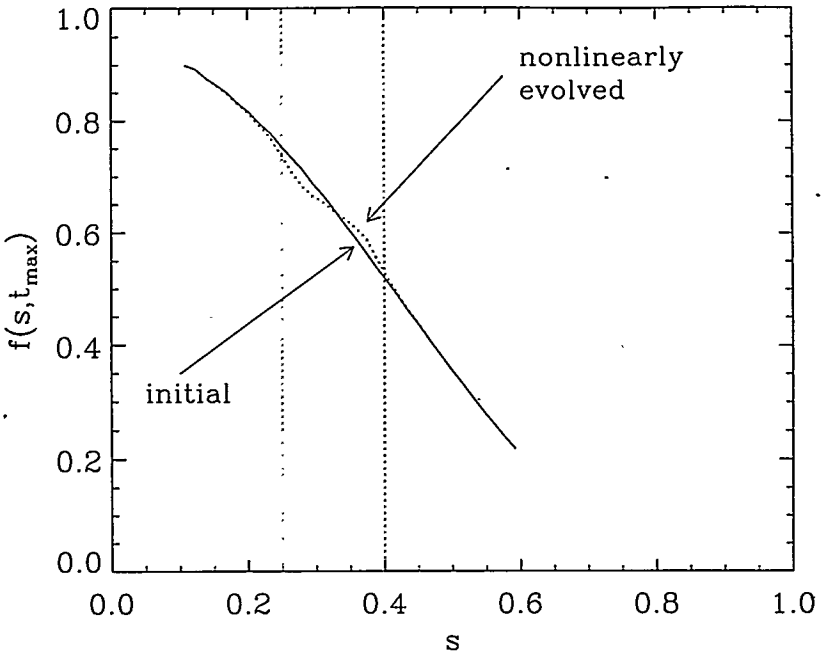
1.0
0.8
0.6
0.4
0.2
0.0
f(s,t_max)
0.0
0.2
0.4
0.6
0.8
1.0
s
nonlinearly
evolved
initial

FIG. 15. Candy